Tilted axis rotation, candidates for chiral bands, and wobbling motion in ^{138}Nd

C. M. Petrache,[1] S. Frauendorf,[2] M. Matsuzaki,[3] R. Leguillon,[1] T. Zerrouki,[1] S. Lunardi,[4] D. Bazzacco,[4] C. A. Ur,[4] E. Farnea,[4] C. Rossi Alvarez,[4] R. Venturelli,[4] and G. de Angelis[5]

[1]*Centre de Spectrométrie Nucléaire et de Spectrométrie de Masse, Université Paris-Sud and CNRS/IN2P3,*
Bâtiment 104-108, F-91405 Orsay, France
[2]*Department of Physics, University of Notre Dame, Notre Dame, Indiana 46556, USA*
[3]*Department of Physics, Fukuoka University of Education, Munakata, Fukuoka 811-4192, Japan*
[4]*Dipartimento di Fisica dell'Universit and INFN Sezione di Padova, I-35131 Padova, Italy*
[5]*INFN Laboratori Nazionali di Legnaro, I-35020 Legnaro, Italy*

High-spin states in ^{138}Nd were investigated using the reaction ^{94}Zr(^{48}Ca, $4n$), detecting coincident γ rays with the GASP spectrometer. A rich level scheme was constructed including four bands of negative parity at low spins, eight bands of dipole transitions, and eight bands of quadrupole transitions at medium spins. The cranked shell model and the tilted-axis cranking model are used to assign configurations to the observed bands, where zero pairing is assumed. For selected configurations the case of finite pairing is also considered. A consistent notation for configuration assignment that applies for both zero and finite pairing is introduced. The observed bands are interpreted as rotation around the short and long principal axes (quadrupole bands), as well as around a tilted axis (dipole bands). The dipole bands have an intermediate character, between magnetic and collective electric rotation. A pair of dipole bands is identified as candidates for chiral partners. The possible existence of the wobbling mode at low deformation and medium spins is discussed. The consistent interpretation of the multitude of observed bands strongly supports the existence of stable triaxial deformation at medium spins in ^{138}Nd.

I. INTRODUCTION

The existence of triaxial nuclei has been the subject of a longstanding debate. The possibility of soft and rigid triaxiality has been proposed very early [1,2], and many theoretical and experimental studies have been devoted to this intriguing phenomenon since then. More recently, two unique fingerprints of triaxiality in nuclei have been intensively studied: the wobbling motion [3] and the dynamic chirality [4,5]. These exotic types of motion were observed in specific regions of the nuclear chart: the wobbling motion in the odd-even Lu nuclei with $A \sim 160$ [6] and the chirality primarily in the odd-odd and odd-even nuclei with $A \sim 130$ nuclei [4,7,8]. In the nuclei $^{136-140}$Nd, surrounding the subject of the present paper, the rotational bands at medium and high spins have been successfully interpreted with model calculations based on triaxial shapes [9–13]. In the same mass region nearly degenerate bands with the same spin and parity have been observed, and interpreted as chiral partners (for example ^{134}Pr and ^{135}Nd [4,7,8]). As a primary prerequisite of chirality, the nuclides must have a triaxial shape. The evolution from axial to triaxial shape in ^{136}Nd was discussed in Ref. [9]. The authors of Refs. [11–13] proposed stable triaxiality at high-spin in ^{138,139,140}Nd. A highly deformed band in ^{138}Nd and a superdeformed (SD) band in ^{140}Nd were suggested in Refs. [14,15], respectively.

The present study is devoted to ^{138}Nd and reports states at low and medium spins. The level scheme has been constructed up to much higher spins and excitation energy of around 45$\hbar$ and 24 MeV, respectively. Many new levels were established at low and medium spins, leading to a very rich and rather complete level scheme. Of particular interest are one band of

quadrupole transitions which is interpreted as manifestation of the wobbling mode and several dipole bands which are interpreted as rotation around a tilted axis of the intrinsic reference system. Such a variety of excitations in a single nucleus, most of them being explained by assuming a triaxial shape, makes ^{138}Nd one of the best studied examples of triaxiality at medium and high spins.

The level structure of ^{138}Nd was first studied using a (p, $4n$) reaction by Yoshikawa [17] and through the β^+ decay of ^{138}Pm by Deslauriers *et al.* [18]. High-spin states in ^{138}Nd have been previously studied by Müller-Veggian *et al.* [19,20] and de Angelis *et al.* [21] up to spin 19$\hbar$ and 21$\hbar$, respectively. More recently, four high-spin bands were observed in ^{138}Nd using the ^{94}Zr(^{48}Ca, $4n$) reaction at an energy of 195 MeV [11]. Gamma-ray coincidences were measured with the 8π spectrometer consisting of 20 Ge detectors with anti-Compton shields and an inner ball of 71 BGO scintillator detectors. Two of the four observed bands were linked to low-lying states. A highly deformed band was also reported from a GASP experiment using the same ^{94}Zr(^{48}Ca, $4n$) reaction at beam energies of 188 and 195 MeV [14]. The linking transitions of the highly deformed band to low-lying states were not identified, and therefore the spins and parity were not determined experimentally.

The details of the experimental setup are briefly discussed in Sec. II. The results including the level scheme are presented in Sec. III. The configurations of the different bands are discussed in Sec. IV on the basis of theoretical calculations using the Cranked Shell Model (CSM) [22], the Tilted Axis Cranking (TAC) model [5,23,24], and the Cranked Nilsson + BCS formalism [25–27]. Finally, the configuration assignments and a summary are given in Secs. V and VI.

II. EXPERIMENTAL DETAILS

High-spin states in ^{138}Nd have been populated via the ^{94}Zr(^{48}Ca, 4n) reaction at beam energies of 188 and 195 MeV. The target consisted of a stack of two self-supporting ^{94}Zr foils of 400 μg/cm^2 thickness each. The ^{48}Ca beam of $3-4$ pnA was provided by the XTU Tandem accelerator of the Laboratori Nazionali di Legnaro. The GASP array with 40 Compton-suppressed Ge detectors and the 80-element BGO ball has been used for a standard coincidence measurement. Events were collected when at least three suppressed Ge detectors and three BGO detectors of the inner ball fired in coincidence. A total of 1.9 x 10^9 triple- or higher-fold events have been collected. The ^{138}Nd nucleus was one of the most intensely populated in the reaction, with about 30% of the fusion cross section.

In order to search for discrete bands we have produced a three-dimensional histogram of energies from triple-coincident γ-ray events, from which we extracted γ-γ matrices gated on selected transitions of ^{138}Nd. From the coincidence relationships we could assign to ^{138}Nd many new transitions, which are organized in several bands. The transition multipolarities have been extracted from the Directional Correlation of Oriented states (DCO) ratios using the procedure described in Ref. [7].

III. RESULTS AND LEVEL SCHEME

The level scheme of ^{138}Nd is shown in Fig. 1. Most of the observed transitions were grouped in four bands of negative parity at low spins (N1–N4), eight bands at medium spins (L1–L8), and eight bands of dipole transitions (D1–D8). We also draw the levels which were assigned to the γ band from β-decay studies [18], even though they were not observed in the present experiment. The energies, relative intensities, DCO ratios, and spin-parity assignments of the observed transitions are reported in Table I. The spectroscopic data on ^{138}Nd are very much enriched with respect to the previous studies [11, 17–21]. The newly constructed level scheme will be discussed separately for the bands of quadrupole and dipole transitions.

A. Ground-state band and the negative-parity states

The ground-state band is yrast up to spin 6$^+$. The 69-keV transition connecting the 10$^+$ isomer to the 8$^+$ state was not observed in our measurement. Evidence for the existence of this transition was given in Ref. [20], where the measured energy was 66.9 keV. We add credibility to the 69-keV value, which results from the difference between the 8$^+$ and 10$^+$ states whose energies are well established through the connecting transitions between many high-spin states of the present level scheme which were not observed in Ref. [20]. The only other observed transition populating the 8$^+$ state is the newly observed 1238-keV transition de-exciting the dipole band D4.

Most of the populated states decay through γ cascades involving the two 556.7- and 557.3-keV members of the 557-keV triplet peak. We observed all the previously reported transitions between the negative-parity states and toward the

ground-state band and their positions in the level scheme are confirmed, with the exception of the 563-, 839-, and 1022-keV transitions. The 563-keV transition belongs to ^{138}Nd but de-excites the 20$^+$ state at 7764 keV toward which decays the strongest high-spin rotational band, which will be published separately [16]. The 839- and 1022-keV transitions are in mutual coincidence and were placed in the newly observed band N2. We observed several new transitions between the low-lying negative-parity states with energies of 144, 187, 359, 558, and 577 keV, and we inverted the order of the transitions in the cascades 373–677 and 391–659 keV. We also changed the parity of the two nonyrast 8$^+$ states to negative parity. The three newly observed transitions with energies of 187, 558, and 577 keV firmly define the new 10$^-$ state at 3556 keV, on top of which are placed the 839-, 1022-, and 992-keV quadrupole transitions of band N2. The 8$^-$ state at 2998 keV has an unbalanced intensity, with twice more intensity feeding the state than the intensity de-exciting it. This can be an indication of the isomeric character of the 8$^-$ state with a lifetime of the order of several nanoseconds, but this was not possible to deduce from the present data set.

The high-lying levels of these bands are nonyrast and therefore are very weakly populated. The most intense are the N3 and N4 bands, which are strongly populated from the 10$^+$ state through the 329- and 454-keV transitions, respectively. We identified one more transition on top of both bands N1 and N2, with energies of 953 and 992 keV, respectively. The new 926-keV transition populating the 11$^-$ state of band N4 at 3915 keV is in cascade with the new 736-keV transition de-exciting the 14$^-$ state lying below band D1. We have also identified a new weak transition of 242 keV linking the 16$^-$ state of band D1 to the 15$^-$ state of band N4, which most probably is an $M1/E2$ transition.

An important experimental result is that we confirm the DCO for the 1018-keV transition populating the 13$^-$ state of band N4, which is in agreement with a stretched quadrupole transition. We assign an $E2$ multipolarity to the 1018-keV transition, which therefore de-excites a 15$^-$ state and induces a negative parity for band D1. This result and the observation of the 242-keV transition and of the 736–926 keV cascade linking band D1 to N4 are all arguments in favor of negative parity for band D1, which is in disagreement with Ref. [21], in which a positive-parity was proposed for band D1.

Spectra obtained by doubly gating on selected transitions of the different bands are shown in Fig. 2.

B. The medium-spin bands L1–L5

The most intense band above the 10$^+$ state at 3700 keV is band L1, which was assigned a $\pi h_{11/2}^2$ configuration from the systematics of the 10$^+$ states in the sequence of the $N = 78$ isotones and from the comparison with the ^{136}Ce proton core [21]. In addition to band L1, we identified four more bands, labeled L2–L5, which mainly decay to band L1. Spectra showing the transitions in the different bands are given in Fig. 3.

Some of the transitions connecting bands L2–L5 to band L1 were observed previously [21]. Bands L3 and L4 decay to band L1 via both stretched and nonstretched $E2$ transitions.
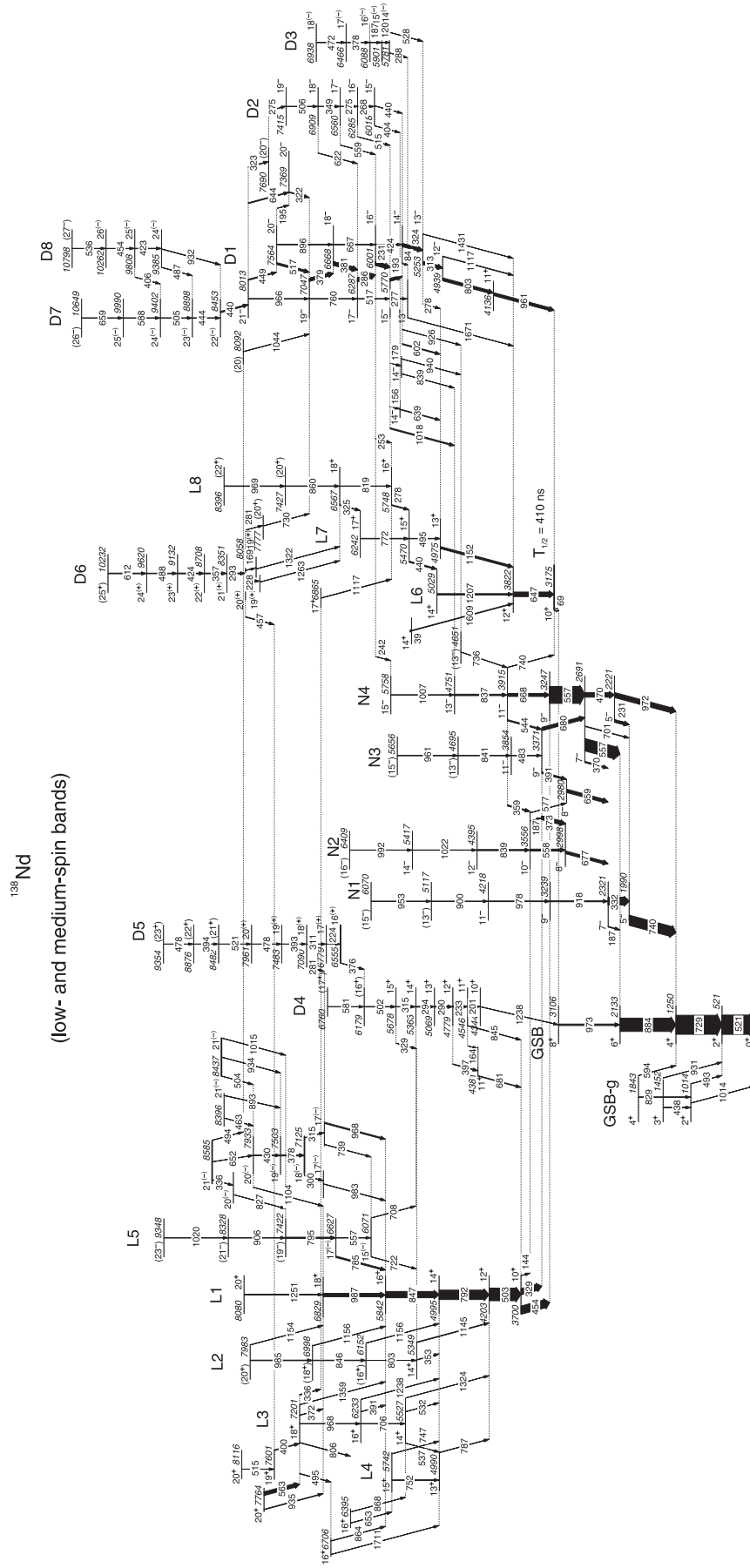
FIG. 1. Partial level scheme of ^{138}Nd showing the low- and medium-spin states.

TABLE I. Energies, intensities, DCO ratios, multipolarities, and spin-parity assignments of γ-ray transitions of ^{138}Nd. The transitions are grouped in bands and the transitions connecting a given band to low-lying states are listed at the end of each band separated by a blank line.

γ-ray energy[a] E_γ (keV)	Intensity[b] I_γ (%)	DCO ratios[c] Gate on $E2$	Gate on $M1$	Multipolarity	$J_i^\pi \to J_f^\pi$
g band					
520.8	100	0.90(5)		$E2$	$2^+ \to 0^+$
728.7	100	0.99(5)		$E2$	$4^+ \to 2^+$
883.9	70	1.03(4)		$E2$	$6^+ \to 4^+$
972.9	7.7		1.74(87)	$E2$	$8^+ \to 6^+$
γ band[d]					
438					$3^+ \to 2^+$
829					$4^+ \to 2^+$
493					$2^+ \to 2^+$
594					$4^+ \to 4^+$
931					$3^+ \to 2^+$
1014					$2^+ \to 0^+$
Band N1					
186.5	3.5				$7^- \to 6^+$
331.5	38.5	1.03(5)		$E2$	$7^- \to 5^-$
918.1	4.9	1.09(28)	1.51(30)	$E2$	$9^- \to 7^-$
978.2	3.7	1.16(38)		$E2$	$11^- \to 9^-$
900.0	2.1				$(13^-) \to 11^-)$
952.6	0.8				$(15^-) \to 13^-)$
740.2	52	0.55(12)		$E1$	$5^- \to 4^+$
Band N2					
558.0	10	0.95(18)		$E2$	$10^- \to 8^-$
838.9	6	0.91(18)		$E2$	$12^- \to 10^-$
1022.2	1.5	1.05(14)		$E2$	$14^- \to 12^-$
991.9	<1				$(16^-) \to 14^-$
186.7	1.2				$10^- \to 9^-$
576.9	1.5				$10^- \to 8^-$
677.0	14.2	0.62(36)		$M1/E2$	$8^- \to 7^-$
Band N3					
483.5	2	0.86(15)		$E2$	$11^- \to 9^-$
840.6	2				$(13^-) \to 11^-$
960.9	1.8				$(15^-) \to (13^-)$
372.7	18.5	0.58(4)		$M1/E2$	$9^- \to 8^-$
391.0	8.2	0.66(10)		$M1/E2$	$9^- \to 8^-$
658.8	16.9	0.52(7)		$M1/E2$	$8^- \to 7^-$
680.0	17.2	0.74(40)		$E2$	$9^- \to 7^-$
Band N4					
469.8	23.4	1.02(13)		$E2$	$7^- \to 5^-$
556.7	88.6	0.96(12)		$E2$	$9^- \to 7^-$
668.0	16	1.09(9)		$E2$	$11^- \to 9^-$
836.7	7.4	0.88(32)	1.47(17)	$E2$	$13^- \to 11^-$
1007.1	3.0	0.90(25)		$E2$	$15^- \to 13^-$
230.7	12.5				$5^- \to 5^-$
359.0	6	0.76(49)		$M1/E2$	$11^- \to 10^-$
369.8	6.6	1.08(10)		$M1/E2$	$7^- \to 7^-$
543.9	6.3	1.00(60)		$E2$	$11^- \to 9^-$
557.3	63		1.21(8)	$E1/M2$	$7^- \to 6^+$
701.2	2.6				$7^- \to 5^-$
740.4	7				$11^- \to 10^+$
971.7	26	0.57(7)		$E1$	$5^- \to 4^+$
Band L1					
502.8	64	0.87(10)	1.55(9)	$E2$	$12^+ \to 10^+$
792.1	49.4	1.10(15)		$E2$	$14^+ \to 12^+$

TABLE I. (*Continued.*)

γ-ray energy[a]	Intensity[b]	DCO ratios[c]		Multipolarity	$J_i^\pi \to J_f^\pi$
E_γ (keV)	I_γ (%)	Gate on $E2$	Gate on $M1$		
846.7	33		1.95(53)	$E2$	$16^+ \to 14^+$
986.7	17.5	1.01(16)		$E2$	$18^+ \to 16^+$
1251.0	1.3	0.95(44)		$E2$	$20^+ \to 18^+$
143.7	0.7	0.63(35)		$E1/M2$	$10^+ \to 10^-$
329.1	32	0.69(5)		$E1/M2$	$10^+ \to 9^-$
453.6	42	0.62(2)		$E1/M2$	$10^+ \to 9^-$
Band L2					
803.0	0.6				$(16^+) \to 14^+$
845.9	2.5				$(18^+) \to (16^+)$
985.4	3				$(20^+) \to (18^+)$
353.4	2.3	0.74(15)	0.83(50)	$M1/E2$	$14^+ \to 14^+$
1145.4	3.2	1.53(35)	2.88(164)	$E2$	$14^+ \to 12^+$
1154.2	1				$(20^+) \to 18^+$
1155.5	1.8	0.93(40)		$(E2)$	$(18^+) \to 16^+$
1156.4	1.4				$(16^+) \to 14^+$
Band L3					
705.8	0.7		2.08(60)	$E2$	$16^+ \to 14^+$
967.8	2.2				$18^+ \to 16^+$
336.2	3.5		1.37(34)	$M1/E2$	$18^+ \to 17^+$
372.3	2.0				$18^+ \to 18^+$
390.9	1				$16^+ \to 16^+$
399.5	3.5		0.73(15)	$M1/E2$	$19^+ \to 18^+$
494.6	2.4	0.95(11)		$E2$	$18^+ \to 16^+$
514.4	1		1.06(18)	$M1/E2$	$20^+ \to 19^+$
532.1	0.6	1.09(25)		$M1/E2$	$14^+ \to 14^+$
537.3	0.5	0.58(25)		$M1/E2$	$14^+ \to 13^+$
806.2	2.2	0.88(19)		$E2$	$18^+ \to 16^+$
1237.7	1				$16^+ \to 14^+$
1323.7	0.4				$14^+ \to 12^+$
1358.6	1.0	0.88(20)		$E2$	$18^+ \to 16^+$
Band L4					
752.3	0.5				$15^+ \to 13^+$
653.1	1	0.29(19)		$M1/E2$	$16^+ \to 15^+$
747.0	1.2	0.27(4)		$M1/E2$	$15^+ \to 14^+$
786.8	1.9		0.50(20)	$M1/E2$	$13^+ \to 12^+$
864.5	2				$16^+ \to 16^+$
867.8	0.7				$16^+ \to 14^+$
1117.4	2		0.57(25)	$M1/E2$	$17^+ \to 16^+$
1711.4	0.7				$16^+ \to 14^+$
Band L5					
556.6	0.25				$17^{(-)} \to 15^{(-)}$
794.6	6.9		1.99(175)	$(E2)$	$(19^-) \to 17^{(-)}$
906.4	2.5		1.33(40)	$(E2)$	$(21^-) \to (19^-)$
1019.8	1.6				$(23^-) \to (21^-)$
708.4	0.06		0.52(30)	$(E1)$	$15^{(-)} \to 14^+$
722.4	0.18		1.38(28)	$(E1/M2)$	$15^{(-)} \to 14^+$
785.4	7.4	0.68(6)		$(E1/M2)$	$17^{(-)} \to 16^+$
Band L6					
646.9	24	0.87(13)	2.4(4)	$E2$	$12^+ \to 10^+$
1206.7	7.2	1.00(11)		$E2$	$14^+ \to 12^+$
Band L7					
494.7	2.2	0.96(40)		$E2$	$15^+ \to 13^+$
772.4	2.7	0.97(31)		$E2$	$17^+ \to 15^+$
38.7	<1				$15^+ \to 14^+$

TABLE I. (*Continued.*)

γ-ray energy[a] E_γ (keV)	Intensity[b] I_γ (%)	DCO ratios[c] Gate on $E2$	Gate on $M1$	Multipolarity	$J_i^\pi \to J_f^\pi$
440.2	6.4	0.61(17)		$M1/E2$	$15^+ \to 14^+$
1152.3	10.7	0.37(4)		$M1/E2$	$13^+ \to 12^+$
Band L8					
818.6	1.9		1.74(27)	$E2$	$18^+ \to 16^+$
859.7	2.6		1.35(55)	$(E2)$	$(20^+) \to 18^+$
968.9	2.9	0.94(59)		$(E2)$	$(22^+) \to (20^+)$
278.4	4.0	0.36(7)		$M1/E2$	$16^+ \to 15^+$
324.8	3	0.39(12)		$M1/E2$	$18^+ \to 17^+$
1608.7	3.4	0.90(15)	1.28(28)	$E2$	$14^+ \to 12^+$
Band D1					
83.6	0.16				$14^- \to (13^-)$
193.4	12.3	0.60(7)	0.90(13)	$M1/E2$	$15^- \to 14^-$
277.0	0.3				$15^- \to 13^-$
230.6	18.2	0.57(9)	0.87(4)	$M1/E2$	$16^- \to 15^-$
286.2	21.4	0.61(5)		$M1/E2$	$17^- \to 16^-$
380.8	19	0.58(5)		$M1/E2$	$18^- \to 17^-$
378.8	16	0.54(7)		$M1/E2$	$19^- \to 18^-$
517.5	10		0.91(8)	$M1/E2$	$20^- \to 19^-$
448.7	5.3		0.83(5)	$M1/E2$	$21^- \to 20^-$
156.4	1.5	0.63(17)		$M1/E2$	$15^- \to 14^-$
179.0	0.3	0.97(12)		$M1/E2$	$15^- \to 14^-$
193.6	0.8				$20^- \to 20^-$
242.2	0.3				$16^- \to 15^-$
252.9	0.04		0.92(20)	$E1$	$16^- \to 16^+$
278.0	0.7				$13^- \to 13^+$
313.4	15.4	0.77(19)		$M1/E2$	$13^- \to 12^-$
323.2	1.2				$21^- \to (20^-)$
322.4	3.3				$20^- \to 19^-$
323.7	15.8	0.60(10)		$M1/E2$	$14^- \to 13^-$
424.0	1				$16^- \to 14^-$
516.7	2.1				$17^- \to 15^-$
602.2	4.9	0.52(6)		$E1$	$14^- \to 13^+$
639.3	3.4	0.53(15)		$E1$	$14^- \to 13^+$
643.6	4.4		1.04(15)	$M1/E2$	$21^- \to 20^-$
667.0	1				$18^- \to 16^-$
736.4	1				$(13^-) \to 11^-$
759.6	1				$19^- \to 17^-$
803.1	15		0.93(9)	$E1$	$12^- \to 11^+$
838.8	0.2				$14^- \to 13^-$
896.3	0.6				$20^- \to 18^-$
925.6	1.2				$14^- \to (13^-)$
939.5	0.2				$14^- \to (13^-)$
961.1	15		0.61(5)	$M1/E2$	$11^+ \to 10^+$
966.2	0.8				$21^- \to 19^-$
1018.3	5.9	1.06(20)	1.8(8)	$E2$	$15^- \to 13^-$
1117.3	2.6	0.75(15)		$E1/M2$	$12^- \to 12^+$
1430.9	1				$13^- \to 12^+$
1670.9	1.2	0.79(47)	1.45(45)	$(E1)$	$(13^-) \to 12^+$
Band D2					
267.5	0.13		1.05(10)	$M1/E2$	$16^- \to 15^-$
275.2	1.9		1.06(10)	$M1/E2$	$17^- \to 16^-$
349.0	1.0		0.95(10)	$M1/E2$	$18^- \to 17^-$
505.6	0.8		0.86(34)	$M1/E2$	$19^- \to 18^-$
275.1	<1				$(20^-) \to 19^-$
403.5	<0.1		0.97(25)	$M1/E2$	$15^- \to 14^-$

TABLE I. (*Continued.*)

γ-ray energy[a]	Intensity[b]	DCO ratios[c]		Multipolarity	$J_i^\pi \to J_f^\pi$
E_γ (keV)	I_γ (%)	Gate on $E2$	Gate on $M1$		
440.1	<0.1		0.94(20)	$M1/E2$	$15^- \to 14^-$
514.6	1.1		0.86(23)	$M1/E2$	$16^- \to 15^-$
559.2	0.3		0.72(36)	$M1/E2$	$17^- \to 16^-$
622.0	<0.06				$18^- \to 17^-$
Band D3					
120.3	0.1		1.19(16)	$M1/E2$	$15^{(-)} \to 14^{(-)}$
186.8	1.2		1.44(36)	$M1/E2$	$16^{(-)} \to 15^{(-)}$
377.6	1		0.75(8)	$M1/E2$	$17^{(-)} \to 16^{(-)}$
471.8	0.1		0.86(25)	$M1/E2$	$18^{(-)} \to 17^{(-)}$
288.0	1.2		0.88(19)	$(M1/E2)$	$14^{(-)} \to (13^-)$
528.2	0.5		1.00(35)	$(M1/E2)$	$14^{(-)} \to 13^-$
Band D4					
201.2	2.5	0.73(25)		$M1/E2$	$11^+ \to 10^+$
233.0	4.9		0.90(23)	$M1/E2$	$12^+ \to 11^+$
290.3	4.7		0.93(10)	$M1/E2$	$13^+ \to 12^+$
293.8	4.0		0.84(15)	$M1/E2$	$14^+ \to 13^+$
314.9	1.8		1.12(32)	$M1/E2$	$15^+ \to 14^+$
501.6	2.8				$(16^+) \to 15^+$
580.6	0.9				$(17^+) \to (16^+)$
164.1	0.2		0.46(18)	$M1/E2$	$11^+ \to 11^+$
328.9	1				$15^+ \to 14^+$
397.3	2.8		0.78(11)	$M1/E2$	$12^+ \to 11^+$
681.2	3.0		0.77(12)	$M1/E2$	$11^+ \to 10^+$
845.0	1.9				$11^+ \to 10^+$
1238.0	0.7		1.96(98)	$E2$	$10^+ \to 8^+$
Band D5					
224.4	1.1		0.97(15)	$M1/E2$	$17^{(+)} \to 16^{(+)}$
310.6	1.1		1.09(16)	$M1/E2$	$18^{(+)} \to 17^{(+)}$
393.4	1.0		1.00(12)	$M1/E2$	$19^{(+)} \to 18^{(+)}$
394.4	0.2		1.00(12)	$(M1/E2)$	$(22^+) \to (21^+)$
477.9	0.2		1.00(55)	$(M1/E2)$	$(23^+) \to (22^+)$
478.0	0.5		1.00(55)	$M1/E2$	$20^{(+)} \to 19^{(+)}$
521.3	<0.2				$(21^+) \to 20^{(+)}$
280.9	0.7		0.99(20)	$(E1)$	$18^{(+)} \to 17^{(-)}$
376.1	0.5		1.32(47)	$(M1/E2)$	$16^{(+)} \to (16^+)$
Band D6					
228.0	1.5		1.22(18)	$M1/E2$	$20^{(+)} \to 19^{(+)}$
293.4	3.9	0.20(14)	1.00(60)	$M1/E2$	$21^{(+)} \to 20^{(+)}$
356.7	3.8	0.27(30)		$M1/E2$	$22^{(+)} \to 21^{(+)}$
424.4	4.3		1.00(15)	$M1/E2$	$23^{(+)} \to 22^{(+)}$
487.9	3		0.91(15)	$M1/E2$	$24^{(+)} \to 23^{(+)}$
611.6	3.7				$(25^+) \to 24^{(+)}$
169.9	1.0			$(M1/E2)$	$20^{(+)} \to 19^{(+)}$
281.4	0.06				$20^- \to (20^+)$
456.9	2.4		0.95(12)	$(M1/E2)$	$20^{(+)} \to 19^+$
730.3	0.06				$(20^+) \to 19^-$
1262.8	1.1	0.40(28)	0.65(52)	$(M1/E2)$	$19^{(+)} \to 18^+$
1322.4	1			$(M1/E2)$	$19^{(+)} \to 18^+$
Band D7					
444.4	2.7		0.87(5)	$M1/E2$	$23^{(-)} \to 22^{(-)}$
504.6	2.3		1.05(25)	$M1/E2$	$24^{(-)} \to 23^{(-)}$
587.7	1.5		1.06(35)	$M1/E2$	$25^{(-)} \to 24^{(-)}$
659.3	<1				$(26^-) \to 25^{(-)}$
439.9	6.7		0.87(5)	$M1/E2$	$22^{(-)} \to 21^-$

TABLE I. (*Continued.*)

γ-ray energy[a] E_γ (keV)	Intensity[b] I_γ (%)	DCO ratios[c] Gate on $E2$	Gate on $M1$	Multipolarity	$J_i^\pi \to J_f^\pi$
Band D8					
423.4	2.0		0.95(20)	$M1/E2$	$25^{(-)} \to 24^{(-)}$
454.4	0.8		1.12(20)	$M1/E2$	$26^{(-)} \to 25^{(-)}$
536.0	<0.3				$(27^-) \to 26^{(-)}$
406	<0.1				$25^{(-)} \to 24^{(-)}$
487.8	<1		1.06(16)	$M1/E2$	$24^{(-)} \to 23^{(-)}$
931.5	<2				$24^{(-)} \to 22^{(-)}$
High-spin negative-parity levels					
300.0	1.0		1.41(50)	$M1/E2$	$18^{(-)} \to 17^{(-)}$
315.2	1.8		1.04(25)	$M1/E2$	$18^{(-)} \to 17^{(-)}$
335.9	0.2	0.61(5)		$M1/E2$	$21^{(-)} \to 20^{(-)}$
378.0	5.9	1.11(11)	0.73(15)	$M1/E2$	$19^{(-)} \to 18^{(-)}$
430.4	2.3		0.68(17)	$M1/E2$	$20^{(-)} \to 19^{(-)}$
462.5	1.2		0.94(7)	$M1/E2$	$21^{(-)} \to 20^{(-)}$
493.8	0.37				$21^- \to (20)$
651.9	1.1		1.10(25)	$M1/E2$	$21^{(-)} \to 20^{(-)}$
738.9	1.0				$17^{(-)} \to 15^{(-)}$
826.7	0.2		1.65(81)	$M1/E2$	$20^{(-)} \to (19^-)$
893.1	0.8				$21^{(-)} \to 19^{(-)}$
934.3					$21^{(-)} \to 19^{(-)}$
968.5	6.3	0.50(12)		$(E1)$	$17^{(-)} \to 16^+$
983.1	1.5				$17^{(-)} \to 16^+$
1015.2					$21^{(-)} \to (19^-)$
1044.7	0.4				$(20) \to 19^-$
1104.1					$20^{(-)} \to 18^+$

[a]The error on the transition energies is 0.2 keV for transitions below 1000 keV and intensities larger than 5% of the ^{138}Nd reaction channel, 0.5 keV for transitions above 1000 keV and intensities lower than 5%, and 1 keV for transitions above 1200 keV and/or weaker than 1%.
[b]Relative intensities are corrected for efficiency. The transition intensities were obtained from a combination of total projection and gated spectra.
[c]The DCO ratios have been deduced from an asymmetric γ-γ coincidence matrix. The tentative spin-parity assignments of the states are given in parentheses.
[d]From National Nuclear Data Center.

Band L5 decays via the 785-keV transition to band L1, but also to bands L2 and D4 via the weak 722- and 708-keV transitions, respectively. The parity of band L5 is uncertain. Therefore it is indicated in parentheses in the level scheme. Because its behavior relative to band L1 is similar to that of the negative-parity bands N1–N4 relative to the ground-state band we tentatively prefer the negative parity.

Several states with spin between $17^{(-)}$ and $21^{(-)}$ which decay to bands L1 and L5 were also observed. We grouped these states together because they may represent negative-parity two-quasiparticle excitations built on the $\pi h_{11/2}^2$ configuration of band L1. They may be the replica of the low-spin negative-parity states, which are two-quasiparticle excitations built on the ground-state configuration. The intense high-spin triaxial band T3 decays to these states [16].

C. The positive-parity bands L6−L8

The next most intense structure above spin 10^+ is band L6, which is built on the yrast 10^+ isomer with $T_{1/2} = 0.41$ μs assigned to the $\nu h_{11/2}^2$ configuration [21]. Figure 4 shows the transitions of the different bands.

We confirm nearly all transitions observed in Ref. [21] and add several new transitions. The 1430-keV $13^- \to 12^+$ and 1671-keV $(13^-) \to 12^+$ transitions connect the nonyrast negative-parity states with the yrast 12^+ state. We added the 969-keV transition on top of band L8. It is interesting to notice the difference between the irregular structures built on the 10^+ isomer, which has assigned to a $\nu h_{11/2}^2$ two-neutron configuration, and those built on the $\pi h_{11/2}^2$ two-proton configuration, which are much more regular, as expected for collective rotational bands. The structures related to the 10^+ isomer are more fragmented. Note the strong population of the 11^+ state at 4136 keV.

D. The dipole bands

A particular feature of the level scheme of ^{138}Nd at medium spins is the existence of eight cascades of dipole transitions, which we call the dipole bands and label D1–D8. Only band D1 was observed previously [21]. The seven newly observed bands are weaker, but they are all connected to low-lying states and therefore have spin-parity assignments. Spectra showing the transitions in the different bands are given in Figs. 5 and 6.
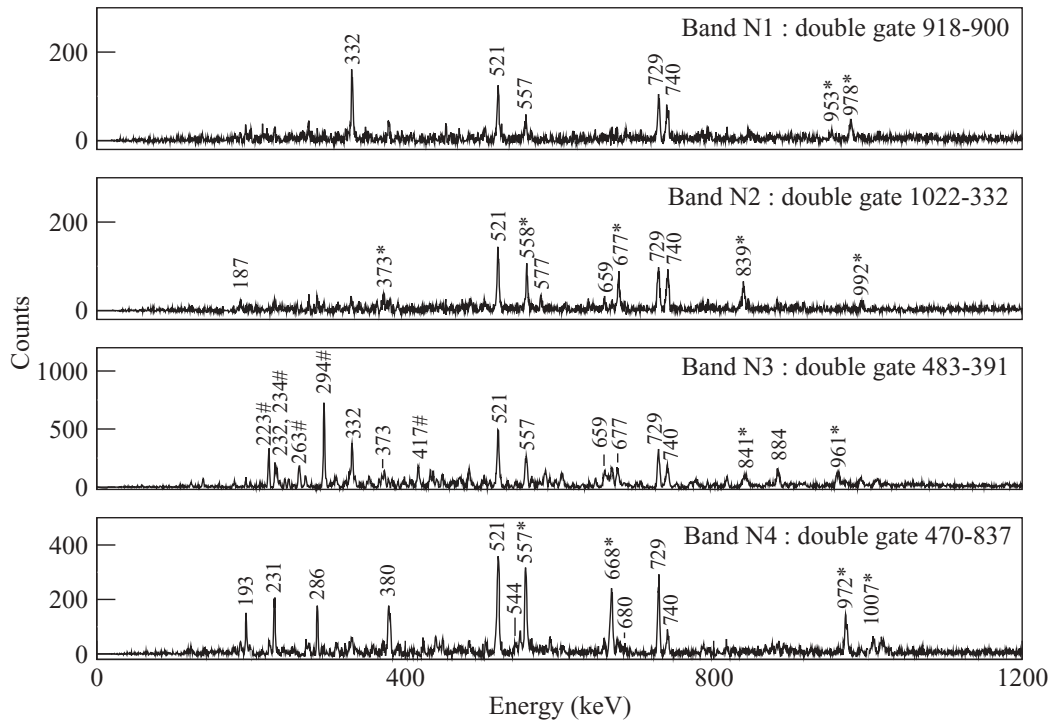
FIG. 2. Double-gated spectra for the negative-parity bands N1, N2, N3, and N4 in ^{138}Nd. The spectra were obtained by summing single-gated spectra by selected transitions of each band. The transitions marked with asterisks represent the members of the band, while the peaks marked with a # are contaminants from other nuclei.
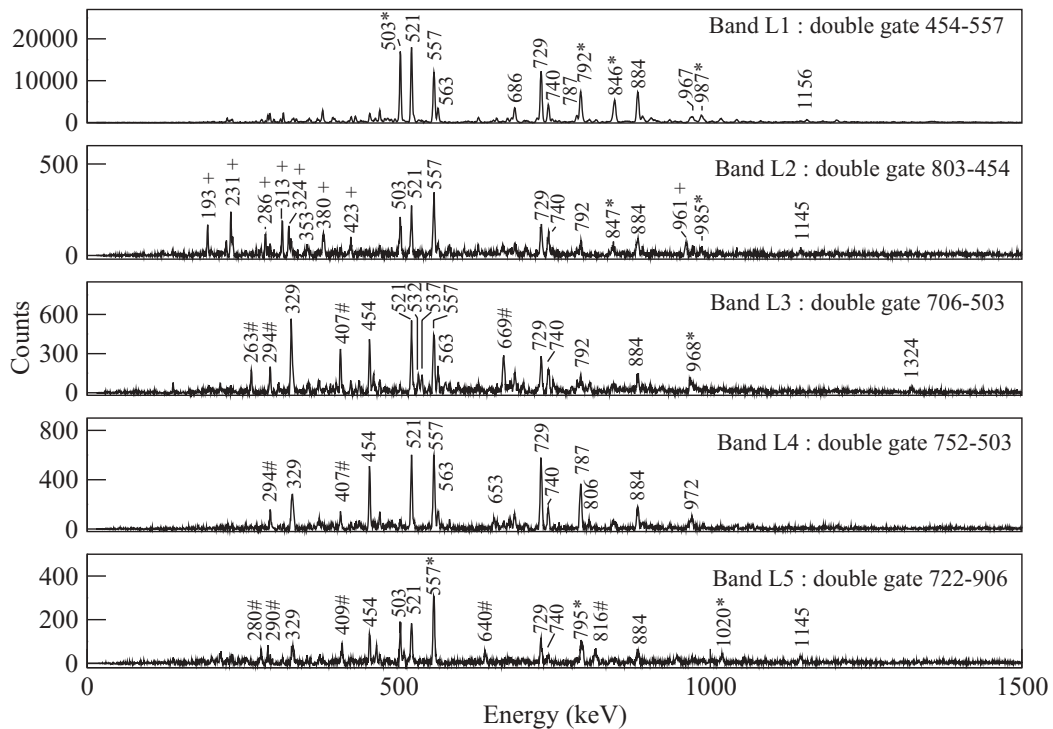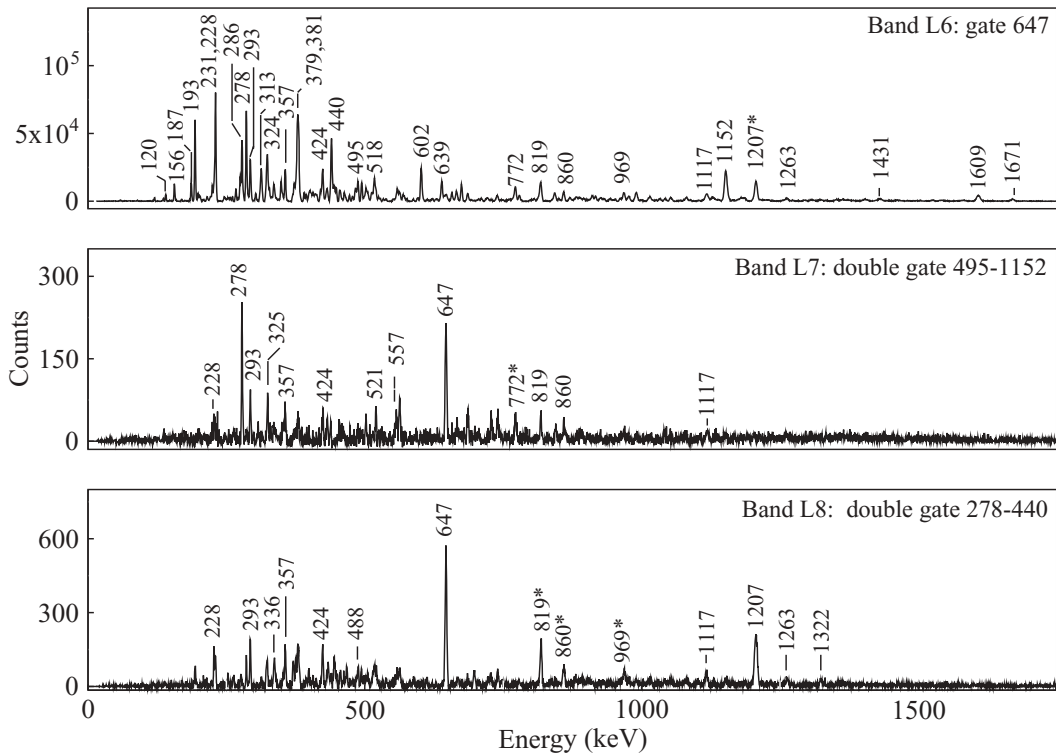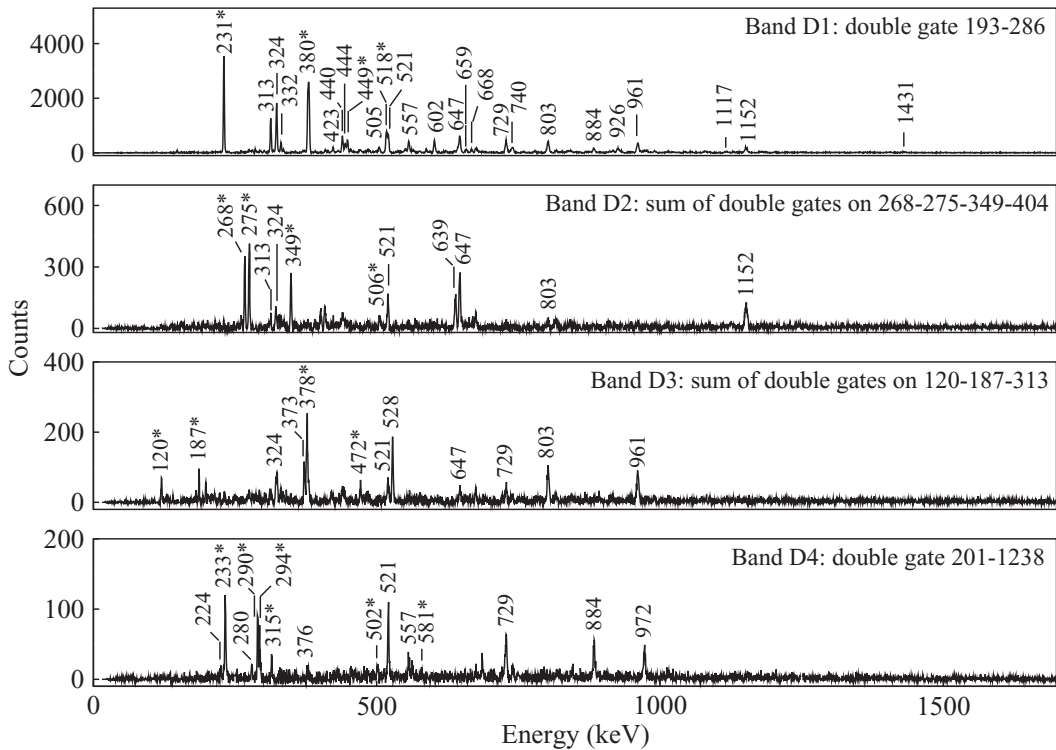

FIG. 3. Double-gated spectra for the bands L1–L5 in ^{138}Nd. The spectra were obtained by summing single-gated spectra by selected transitions of each band. The transit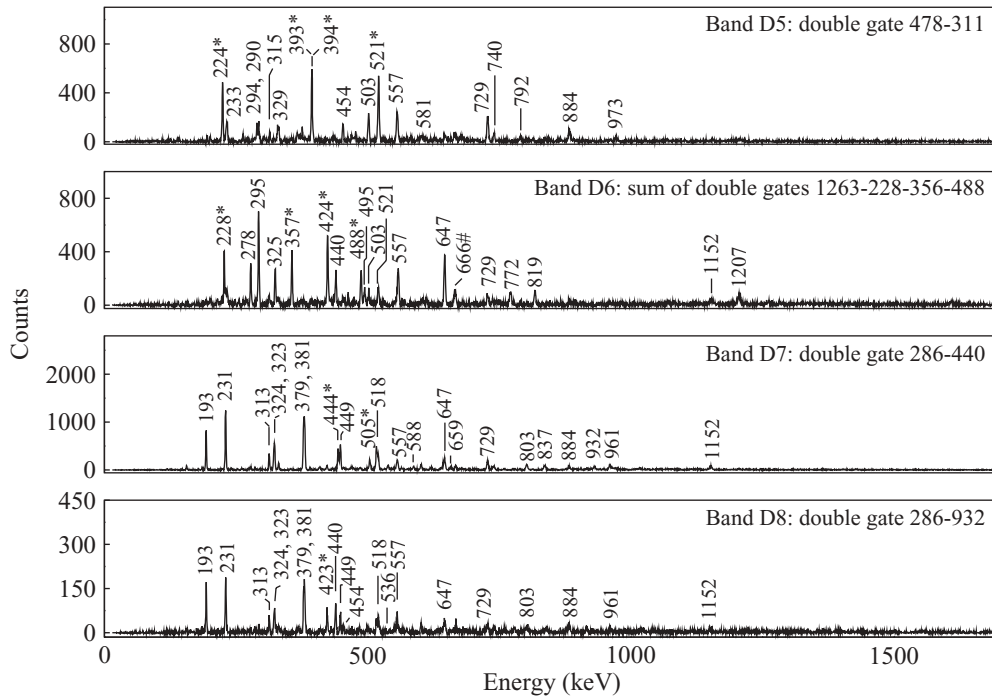ions marked with asterisks represent the members of the band, the peaks marked with a + are members of band D1 which appear in the spectrum of band L2 because they are in cascade with the 803- and 454-keV transitions, and the peaks marked with a # are contaminants from other nuclei.

FIG. 4. Double-gated spectra for the positive-parity L6, L7, and L8 bands in ^{138}Nd. The spectra were obtained by summing single-gated spectra by selected transitions of each band. The gates were set on selected transitions of each band. The transitions marked with asterisks represent the members of the band.

FIG. 5. Double-gated spectra for the dipole bands D1 to D4 in ^{138}Nd. The spectra were obtained by summing single-gated spectra by selected transitions of each band. The transitions marked with asterisks represent the members of the band.

FIG. 6. Double-gated spectra for the dipole bands D5 to D8 in ^{138}Nd. The spectra were obtained by summing single-gated spectra by selected transitions of each band. The transitions marked with asterisks represent the members of the band, while the peaks marked with a # are contaminants from other nuclei.

Band D1 is built on the 13^- state and decays mainly to states built on the 10^+ isomer but also to the 13^- and 15^- states of band N4 via the 1018- and 242-keV transitions, respectively, and to the 13^- state at 4841 keV via the 736-keV transition. The quadrupole multipolarity of the 1018-keV transition fixes the parity of band D1 as negative. The quadrupole character of the 1018-keV transition was also observed in Ref. [21], but no parity was assigned to the state with spin 15 at 5770 keV, which is de-excited by this transition. The parity of the next higher state of band D1 with spin 16 was instead assigned as positive. The assignment of Ref. [21] was based on a 973-keV transition to the 10^+ isomer, which is not observed in our experiment. The parity of band D1 was therefore assigned as positive in Ref. [21] and its theoretical interpretation was based on this assignment. We assign instead a negative parity to band D1, which is in agreement with the systematics of bands observed in even-even and odd-even nuclei in this mass region.

Band D2 is built on the 15^- state and decays only to band D1 and to the nonyrast 14^- state at 5614 keV.

Band D3 built on the $14^{(+)}$ state becomes rapidly nonyrast and decays to the group of negative-parity states above the 10^+ isomer via the 288- and 528-keV transitions.

Band D4 is built on the 10^+ state, which is the lowest bandhead spin among the observed dipole bands. It decays to the ground-state band and to band L1. The energy of the 14^+ state is very close to the energy of the 14^+ state of band L2 (with only a 14-keV difference), which apparently leads to the mixing of the two states and explains the existence of the 329-keV $15^+ \rightarrow 14^+$ transition connecting bands D4 and L2, and also the decay of band L5 to the 14^+ states of bands L2 and D4 via the 722- and 708-keV transitions, respectively.

Band D5 is observed above spin $16^{(+)}$. The transition energies increase regularly up to spin 21 and becomes irregular at the highest observed spins. The decay is toward band D4 and the $17^{(-)}$ state at 6810 keV.

Band D6 built on the $19^{(+)}$ state is the most regular one, with an energy difference between successive transitions of around 70 keV, being an ideal candidate for magnetic rotation. It mainly decays to states of band L8 but also to band L3 via the 457-keV transition and to band D1 via the cascade of transitions at 281–730 keV.

Bands D7 and *D8* are observed above spin $22^{(-)}$ and feed the highest observed state of band D1. Band D8 decays only to band D7.

IV. DISCUSSION

The level scheme of ^{138}Nd presents a very rich and complex structure at low and medium spins. We have arranged some of the states in sequences of transitions such that they resemble band structures, but we are aware that this choice is somewhat arbitrary. We will discuss here the majority of the observed states at low and medium spins. Some of them have been observed and already discussed by employing the interacting boson model and Total Routhian Surfaces (TRS) calculations in Ref. [21] and by employing the Cranked Nilsson Strutinsky (CNS) model in Ref. [11].

A. Framework for the CSM and TAC calculations

All but the ground-state band (g band) have at least two quasiparticles excited, which reduces strongly the pair
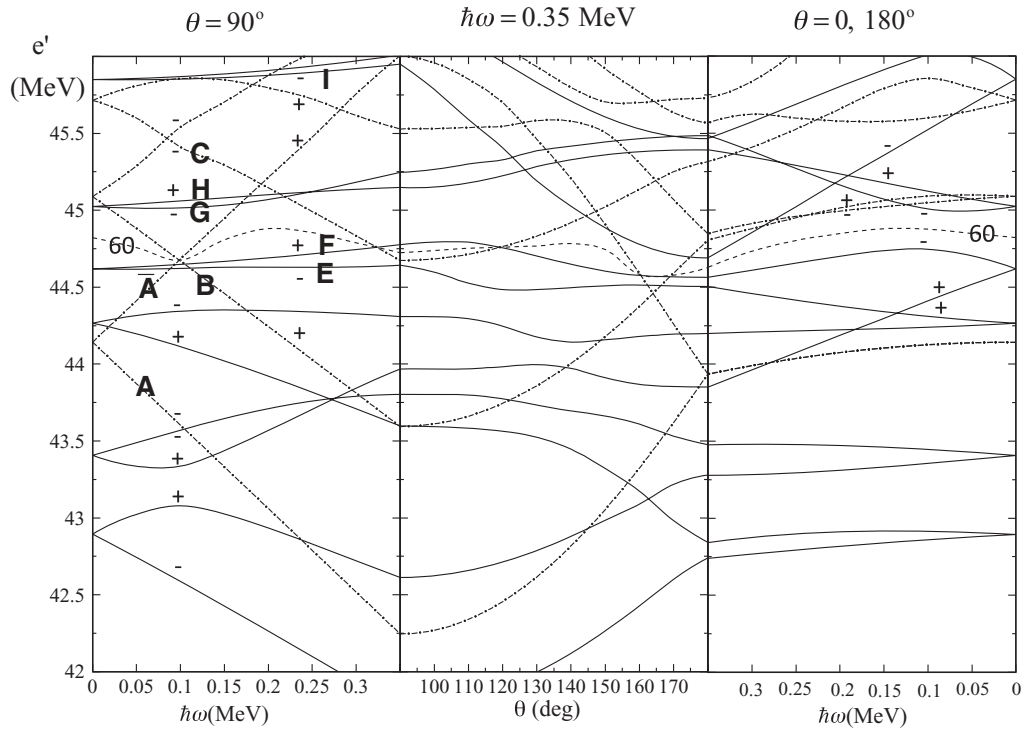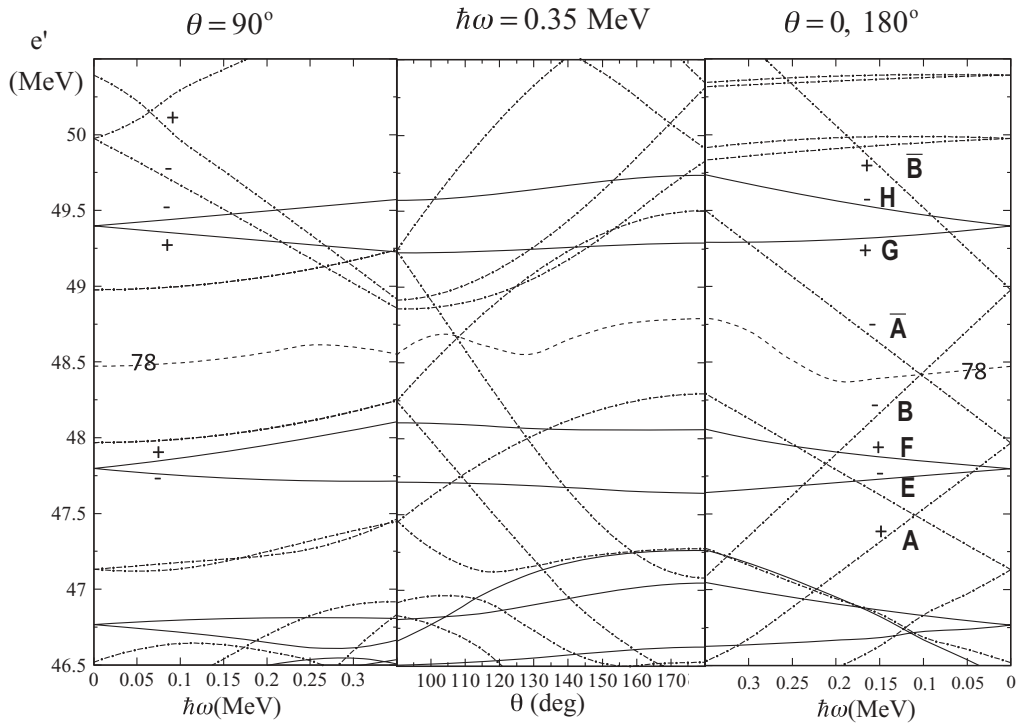
FIG. 7. Single-particle proton Routhians around the Fermi surface of ^{138}Nd calculated for the deformation parameters $\varepsilon_2 = 0.17$ and $\gamma = 30°$. The full line is for $\pi = +$, and the dash-dotted line is for $\pi = -$. In case of principal axis rotation the signatures $\alpha = \pm 1/2$ are indicated by $\pm$, respectively. $\theta = 0$ indicates the long axis ($\gamma = -90°$), and $\theta = 90°$ indicates the short axis ($\gamma = 0°$). The middle panel connects the two axes at the indicated frequency.

FIG. 8. Single-particle neutron Routhians around the Fermi surface of ^{138}Nd calculated for the deformation parameters $\varepsilon_2 = 0.17$ and $\gamma = 30°$. The line and label conventions are similar to those in Fig. 7.

correlations. This allows us to qualitatively interpret the bands in terms of single-particle configurations in the rotating potential. Figures 7 and 8 show the single-particle Routhians calculated by means of the TAC code [24] for a deformation of $\varepsilon_2 = 0.17$ and $\gamma = 30°$, which is a typical value for this mass region [9–13]. The TAC model considers the rotation about an axis that is tilted by the angles θ and ϕ from the principal axes. The long, short, and medium principal axes correspond to (θ, ϕ) equal to $(0°, 0°)$, $(90°, 0°)$, and $(90°, 90°)$, respectively. We will also consider quasiparticle configurations for a strongly reduced pair gap. A compact and unambiguous notation for the configurations is needed that allows one to change from quasiparticle configurations to single-particle configuration as $\Delta \to 0$.

In this paper we apply the Cranked Shell Model (CSM) [22], which classifies the bands as quasiparticle configurations in the rotating potential. With a slight modification it is extended to the zero-pairing version, which classifies the bands as particle-hole configurations. We discuss the band properties using the extension of the CSM to TAC [23] defined by

$$h' = h - \hbar\omega_{\text{rot}} \left(\sin\theta \cos\phi J_x + \sin\theta \sin\phi J_y + \cos\theta J_z \right),$$
(1)

$$h = h_{\text{Nil}} - \Delta_\tau (P_\tau^\dagger + P_\tau) - \lambda_\tau N_\tau,$$
(2)

$$h_{\text{Nil}} = \frac{\mathbf{p}^2}{2M} + \frac{1}{2} M \left(\omega_x^2 x^2 + \omega_y^2 y^2 + \omega_z^2 z^2 \right) + v_{ls} \mathbf{l} \cdot \mathbf{s} + v_{ll} (\mathbf{l}^2 - \langle \mathbf{l}^2 \rangle_{N_{\text{osc}}}).$$
(3)

In Eq. (2), P_τ is the pair annihilation operator, $\tau = 1$ and 2 denote neutron and proton, respectively, and the chemical potentials λ_τ are determined so as to give the correct average particle numbers $\langle N_\tau \rangle$. The oscillator frequencies in Eq. (3) are related to the quadrupole deformation parameters ε_2 and γ in the usual way. Here the orbital angular momentum is defined by the singly stretched coordinates, and v_{ls} and v_{ll} are taken from Ref. [25]. The standard CSM, which allows only for rotation about one of the principal axes [principal axes cranking (PAC)], usually uses x as the rotational axis ($\theta = 90°$, $\phi = 0°$), which is the short axis for $0° < \gamma < 60°$, the medium axis for $-60° < \gamma < 60°$, and the long axis for $-120° < \gamma < -60°$. In the sector $0° < \gamma < 60°$ the short, medium, and long axes correspond to $(\theta, \phi) = (90°, 0°)$, $(90°, 90°)$, and $(0°, 0°)$, respectively.

For zero pairing the CNS notation by Ragnarsson has become quite common [26–28]. It indicates how many particles are in the intruder orbitals and how many in the normal-parity states. We use the $\pi h^n (dg)^m$ notation to indicate that relative to the $Z = 50$ core there are n protons in the $h_{11/2}$ intruder subshell and m protons in the normal-parity states which are a mixture of $d_{5/2}$ and $g_{7/2}$ orbitals. For example, the configuration of band L1 is $\pi h^2 (gd)^8$. For the neutrons it is more convenient to quote the number of neutron holes in the $N = 82$ core. With this notation, the configuration of band L6 is $\nu h^{-2} (dg)^{-2}$.

The CNS notation does not distinguish between the various configurations that are possible for a given $\pi h^n (dg)^m$. It also does not extend well to the case of pairing, because in that case there is pair scattering between the intruder and normal-parity
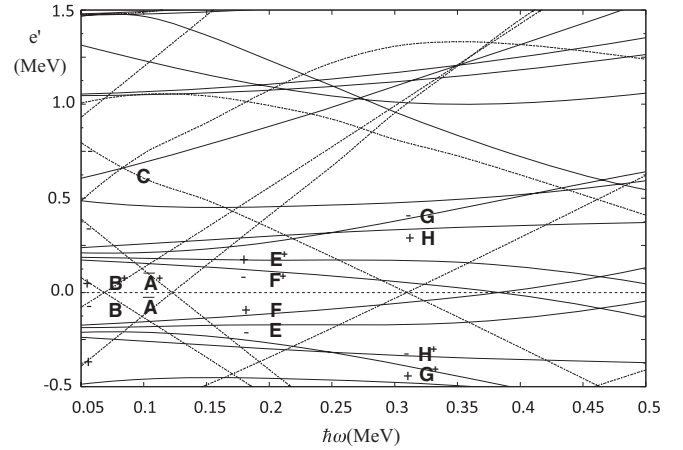

FIG. 9. Quasiproton Routhians around the Fermi surface of ^{138}Nd calculated for $\Delta = 0$ MeV. The deformation parameters are $\varepsilon_2 = 0.17$ and $\gamma = 30°$. Particle excitations are denoted by letters, and hole excitations by a dagger attached to the letter. Only two-quasiparticle excitations combining a particle with a hole are physical.

orbitals, and n and m are not well defined. In CSM calculations one assigns letters to the lowest quasiparticle orbitals for a compact notation [22,29]. The convention is to use A, B, C, and D for the intruder states h, where A is assigned to the lowest state with the favored signature $\alpha = j + 2n$. The letters E, F, G, H, . . . are used for the normal-parity states (dg). We extended the group A, B, C, and D by $\bar{A}$, which is the antialigned (approximately the time reversed) partner of A. We use two ways to specify the unpaired configurations: (i) We specify the configuration by indicating the occupation of the four highest single-particle Routhians. For example, the configuration $\pi 10$, which corresponds to the proton S-band L1,
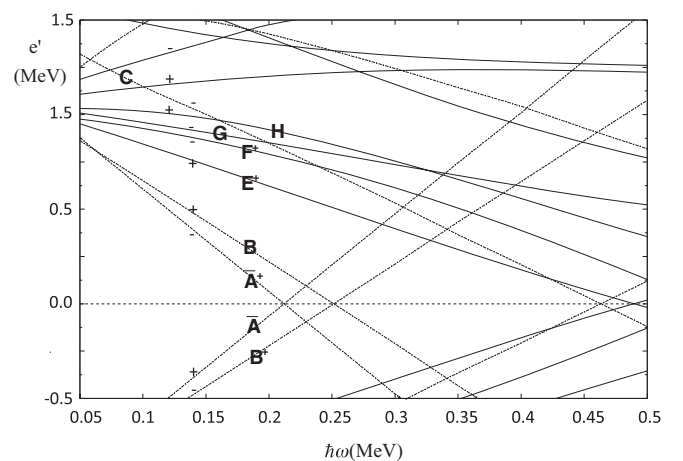

FIG. 10. Quasiproton Routhians around the Fermi surface of ^{138}Nd calculated for $\Delta = 1$ MeV. The deformation parameters are $\varepsilon_2 = 0.17$ and $\gamma = 30°$. Plain letters indicate that the particle character dominates and letters with a dagger indicate that the hole character dominates. For the lowest quasiparticles, the particle and hole components are about the same. The letter code is chosen according to their limit $\Delta \to 0$.

is $\pi ABEF$. (ii) We specify the configuration by indicating the particle-hole excitations relative to the S configuration $\pi 10$, which we use as reference (particle-hole vacuum). For example, the $\pi ABCE$ configuration is generated by exciting F to C, and therefore we will denote it by $\pi F^{-1}C$.

The particle-hole notation naturally extends to the case of finite pairing. In the limit $\Delta \to 0$ a quasiparticle becomes either a particle or a hole. There are twice as many quasiparticle states as single-particle states. Each state has a conjugate partner with opposite energy, which is labeled by a dagger; e.g., $A^{\dagger}$ is the conjugate of A. Conventionally, the Routhians that have negative energy for $\omega = 0$ are labeled by the dagger. However, it is completely open which state of the conjugate pair is given the dagger. Here we use the freedom to additionally indicate whether the quasiparticle is predominantly a particle (no dagger) or a hole (dagger). We indicate this by using the plain letters for quasiparticles that become particles and attach the dagger to the quasiparticles that become holes. For example the quasiparticle G becomes the particle G and the quasiparticle $F^{\dagger}$ becomes the hole F^{-1}. The quasiparticle vacuum is taken as the paired proton S band. The quasiparticle configuration $\pi F^{\dagger}G$ becomes $\pi F^{-1}G$ for zero pairing. For moderate pairing the notation still indicates that $F^{\dagger}$ is predominantly a hole and G predominantly a particle. Of course, for strong pairing the lowest quasiparticles are approximately half particle and half hole. Figures 9 and 10 illustrate the notation.

Table II lists the low-lying quasiparticle configurations and their unpaired particle-hole limits. It is important to point out that certain quasiparticle configurations do not have a zero-pairing limit. For example, $\pi E^{\dagger}F^{\dagger}$ becomes a $Z = 58$

configuration for $\Delta \to 0$ and λ fixed. In principle one could fix this by adjusting λ. However, the CSM uses one set of quasiparticle Routhians for a fixed λ, which ensures that the configurations are mutually orthogonal. This simplicity of the CSM would go away with λ individually adjusted for each configuration, because the configurations are no longer orthogonal. For large pairing the condensate provides a hole pair such that, e.g., $\pi E^{\dagger}F^{\dagger}$ has the right expectation value for Z. For zero (small) pairing $\pi (EF)^{-1}GH$ is the lowest configuration with one proton hole each on E and F. There are more such configurations with the pair on other orbitals. They will combine to generate a pair addition vibration. Analogously, the quasiparticle configuration GH has no $\Delta = 0$ limit and will approach a combination with a pair removal mode.

B. The $\Delta I = 2$ bands

If the nucleus rotates about a principal axis, the signature α is a good quantum number and one observes $\Delta I = 2$ bands with $I = \alpha + 2n$ [22].

1. Zero-pairing CSM calculations

In this section we apply the single-particle version of the CSM [22], which classifies the bands as particle-hole configurations in the rotating potential. Disregarding the g band, we consider only bands with at least two excited quasiparticles, which substantially block the pair correlations. The underlying independent particle approximation of the CSM applies only to relative energies and angular momenta. In contrast to the standard version of CSM in which the g band

TABLE II. Proton and neutron low-lying configurations for $\Delta I = 2$ bands of ^{138}Nd in the particle-hole and quasiparticle notations. The parity, signature, and band assignment are also included.

| Configuration last 4 nucleons	Particle-hole vs S vacuum	Quasiparticles vs S vacuum	Quasiparticles vs g vacuum	$\pi \; \alpha$	Bands
$\pi 0 = A\bar{A}EF$	$\pi B^{-1}\bar{A}$	$\pi B^{\dagger}\bar{A}$	$\pi 0$	$+\;0$	
$\pi 10 = ABEF$	$\pi 10$	$\pi 10$	$\pi \bar{A}^{\dagger}B, \pi h^2$	$+\;0$	L1
$\pi AEFG$	$\pi B^{-1}G$	$\pi B^{\dagger}G$	$\pi \bar{A}^{\dagger}G, \pi h(dg)$	$-\;1$	N3
$\pi AEFH$	$\pi B^{-1}H$	$\pi B^{\dagger}H$	$\pi \bar{A}^{\dagger}H, \pi h(dg)$	$-\;0$	N2
$\pi A\bar{A}BF$	$\pi E^{-1}\bar{A}$	$\pi E^{\dagger}\bar{A}$	$\pi BE^{\dagger}, \pi h(dg)$	$-\;1$	N4
$\pi A\bar{A}BE$	$\pi F^{-1}\bar{A}$	$\pi F^{\dagger}\bar{A}$	$\pi BF^{\dagger}, \pi h(dg)$	$-\;0$	
$\pi ABCE$	$\pi F^{-1}C$	$\pi F^{\dagger}C$	$\pi \bar{A}^{\dagger}BF^{\dagger}C, \pi h^3(dg)$	$-\;1$	L5
$\pi ABCF$	$\pi E^{-1}C$	$\pi E^{\dagger}C$	$\pi \bar{A}^{\dagger}BE^{\dagger}C, \pi h^3(dg)$	$-\;0$	
$\pi ABEG$	$\pi F^{-1}G$	$\pi F^{\dagger}G$	$\pi \bar{A}^{\dagger}BF^{\dagger}G, \pi h^2(dg)^2$	$+\;1$	
$\pi ABEH$	$\pi F^{-1}H$	$\pi F^{\dagger}H$	$\pi \bar{A}^{\dagger}BF^{\dagger}H, \pi h^2(dg)^2$	$+\;0$	L2
$\pi ABFG$	$\pi E^{-1}G$	$\pi E^{\dagger}G$	$\pi \bar{A}^{\dagger}BE^{\dagger}G, \pi h^2(dg)^2$	$+\;0$	L3
$\pi ABFH$	$\pi E^{-1}H$	$\pi E^{\dagger}H$	$\pi \bar{A}^{\dagger}BE^{\dagger}H, \pi h^2(dg)^2$	$+\;1$	L4
	pair removal + pair addition	$\pi E^{\dagger}F^{\dagger}$	$\pi \bar{A}^{\dagger}BE^{\dagger}F^{\dagger}, \pi h^2(dg)^2$	$+\;0$	L2
$\pi ACEF$	$\pi B^{-1}C$	$\pi B^{\dagger}C$	$\pi \bar{A}^{\dagger}C, \pi h^2$	$+\;1$	
$\pi BEFG$	$\pi A^{-1}G$	$\pi A^{\dagger}G$	$\pi BG, h(dg)$	$-\;0$	
$\pi BEFH$	$\pi A^{-1}H$	$\pi A^{\dagger}H$	$\pi BH, \pi(dg)$	$-\;1$	
$\nu 0 = A\bar{A}EF$	$\nu B^{-1}\bar{A}$	$\nu B^{\dagger}\bar{A}$	$\nu 0$	$+\;0$	
$\nu 10 = ABEF$	$\nu 10$	$\nu 10$	$\nu \bar{A}^{\dagger}B, \nu h^2$	$+\;0$	L6
$\nu AEFG$	$\nu B^{-1}G$	$\nu B^{\dagger}G$	$\nu A^{\dagger}G, \nu h(dg)$	$-\;0$	
$\nu AEFH$	$\nu B^{-1}H$	$\nu B^{\dagger}H$	$\nu A^{\dagger}H, \nu h(dg)$	$-\;1$	N1
$\nu A\bar{A}BE$	$\nu F^{-1}\bar{A}$	$\nu F^{\dagger}\bar{A}$	$\nu BF^{\dagger}, \nu h(dg)$	$-\;1$	
$\nu A\bar{A}BF$	$\nu E^{-1}\bar{A}$	$\nu E^{\dagger}\bar{A}$	$\nu BE^{\dagger}, \nu h(dg)$	$-\;0$	
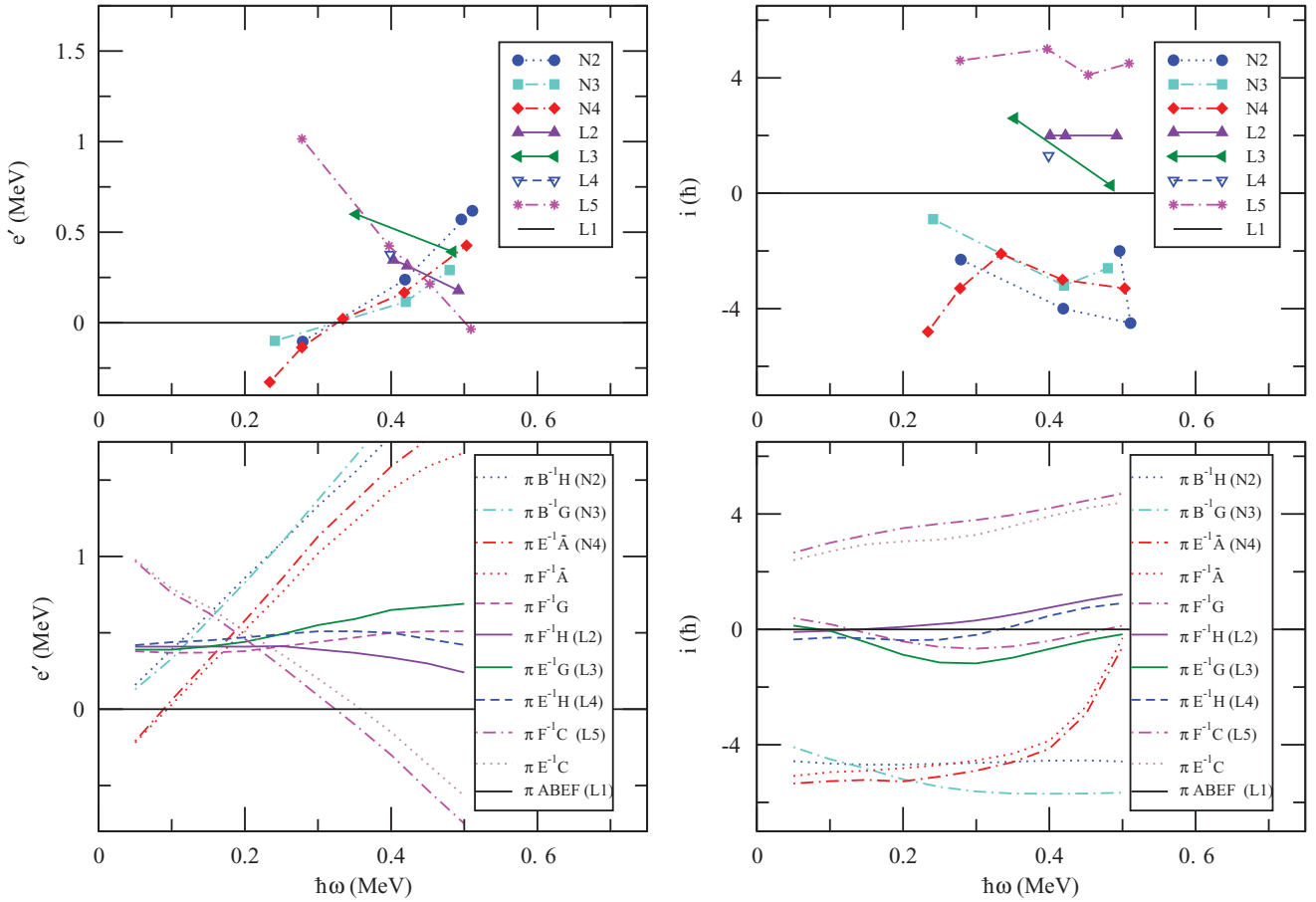
FIG. 11. (Color online) Experimental and calculated Routhians and single-particle alignments relative to band L1 for the $\Delta I = 2$ bands L2–L5 and N2–N4 of ^{138}Nd. Parity and signature (π, α) are indicated by the line type: full $(+, 0)$, dashed $(+, 1)$, dotted $(-, 0)$, and dash-dotted $(-, 1)$.

is used as reference, in this paper we will use the proton S-band L1 as reference.

The experimental particle-hole Routhians e' and alignments i for each band are obtained by following the standard procedure as described, e.g., in Refs. [22,23] for extracting total Routhians $E'(I)$, angular momenta $J(I)$, and frequencies $\omega(I)$ from the level energies $E(I)$, where the expression for $K = 0$ are used. The reference functions $E'_{L1}(\omega)$ and $J_{L1}(\omega)$ are constructed as smooth interpolations between the points $E'(\omega(I))$ and $J(\omega(I))$ obtained for band L1. From the $E_n'(\omega(I))$ and $J_n(\omega(I))$ values of a given band n we subtract the $E_{L1}'(\omega)$ and $J_{L1}(\omega)$ values of band L1 calculated at the same frequencies,

$$e'_n(\omega(I)) = E_n'(\omega(I)) - E_{L1}'(\omega(I)), \qquad (4)$$

$$i_n(\omega(I)) = J_n(\omega(I)) - J_{L1}(\omega(I)). \qquad (5)$$

The experimental Routhians e' and the single-particle alignments i relative to the L1 reference are shown in the upper panels of Figs. 11 and 20 and 21 for the bands of quadrupole and dipole transitions, respectively. The reference band L1 appears as a horizontal line in all figures.

The main features of rotational spectra can be understood in a simple way that has been discussed before (cf., e.g., [5,23]).

There are two $h_{11/2}$ protons which align their angular momenta with the short axis, because this orientation corresponds to maximal overlap of their doughnut-like density distribution with the triaxial core. As a consequence, the $h_{11/2}$ protons favor rotation about the short axis. As seen in the middle panel of Fig. 7, the Routhians A and B have a pronounced minimum at $\theta = 90°$. There are two $h_{11/2}$ neutron holes, which align their angular momenta with the long axis, because this orientation minimizes the overlap with the triaxial core. As a consequence, the $h_{11/2}$ neutron holes favor rotation about the long axis. As seen in the middle panel of Fig. 8, the neutron Routhians $\bar{A}$ and $\bar{B}$ have pronounced maxima at $\theta = 0°$, which means that holes in these two orbitals drive the rotational axis to $\theta = 0°$. Alternatively, one may say that the two neutrons on A and B favor the long axis. The $h_{11/2}$ neutrons on the lower orbitals do not drive the rotational axis significantly, because to each Routhian corresponds a conjugate one (barred) that nearly compensates for the drive. The collective angular momentum originating from the rest of the nucleons is maximal for the medium axis, for which the deviation from axial symmetry is maximal.

The TAC calculations show (see below) that the proton configurations with at least one of the $h_{11/2}$ orbitals A, B, and C occupied combined with the neutrons in the ground configuration $\nu 0 = \nu A \bar{A} E F$ all rotate about the short axis $(90°, 0°)$. Table II

list the low-lying proton configurations, which combined with the neutron g configuration $\nu 0$ generate the regular $\Delta I = 2$ bands. The possible assignments to the observed bands of quadrupole transitions in ^{138}Nd are included as well.

The lower panels of Fig. 11 display the calculated Routhians and single-particle alignments relative to the proton S configuration $\pi 10 = \pi ABEF$ combined with the neutron g configuration $\nu 0$, which is associated with band L1. We calculated the total Routhian $E'(\omega, \theta, \phi, \varepsilon, \gamma)$ as given by the TAC model [24] as a function of the two tilt angles θ, ϕ, the deformation parameter ε, and the triaxiality parameter γ. The calculation shows that the minimum lies always at $(\theta, \phi) = (90°, 0°)$; i.e., the nucleus rotates about the short axis. The minimum of E' (equilibrium deformation) at a frequency of $\hbar\omega = 0.3$ MeV is found for $\varepsilon_2 = 0.15$ and $\gamma = 30°$. We calculated moment of inertia with these parameters. The value of $\mathcal{J}^{(2)} = 17.5\hbar^2$/MeV compares well with the experimental value of $19\hbar^2$/MeV [obtained as the slope of a straight-line fit to the function $J_{L1}(\omega)$]. The negative-parity bands N2, N3, and N4 contain only one rotational aligned $h_{11/2}$ orbital as compared to the reference proton S configuration containing two of them. The panel with experimental single-particle alignments in Fig. 11 shows in fact two groups, one below and one above the zero line corresponding to the L1 reference: the group below is formed by the bands N2–N4, which involve one $h_{11/2}$ orbital, and the group above is formed by the bands L2–L5, which involve two or three aligned $h_{11/2}$ orbitals. The concrete configuration assignment is based on parity, signature, and alignment. Additionally, we took into account that the two bands in ^{136}Nd that correspond to N2 and N3 show a backbend [9]. The backbends are interpreted as the respective configuration changes $\pi B^{-1}G \rightarrow \pi(EF)^{-1}CG$ and $\pi B^{-1}H \rightarrow \pi(EF)^{-1}CH$, which are assisted by the residual pair correlations. The alternative configurations $\pi E^{-1}\bar{A}$ and $\pi F^{-1}\bar{A}$ do not allow such backbends. For this reason, the N2 and N3 bands are assigned to the higher pair of configurations $\pi B^{-1}H$ and $\pi B^{-1}G$ shown in Fig. 11. (The wrong energy order should not be of too much concern, because the neglected correlations may lead to comparable energy shifts.) Exciting one or two protons from (E, F) into (G, H) generates the positive-parity configurations with nearly the same alignment, slightly above the reference, which are assigned to the bands L2, L3, and L4. Band L5 has a higher alignment than L1, which indicates an extra $h_{11/2}$ proton. For this reason we interpret it as $\pi F^{-1}C$. All the bands associated with configurations involving only protons display a regular rotational sequence with a value of $\mathcal{J}^{(2)}$ similar to that of the reference L1.

For the neutron S configuration $\nu 10$ with the two $h_{11/2}$ orbitals A and B occupied, combined with the proton in the g configuration $\pi 0$ we calculated the total Routhian $E'(\omega, \theta, \phi, \varepsilon, \gamma)$ by means of the TAC model [24]. The minimum lies always at $(\theta, \phi) = (0°, 0°)$; i.e., the nucleus rotates about the long axis. The equilibrium deformation for $\hbar\omega = 0.4$ MeV is found at $\varepsilon_2 = 0.14$ and $\gamma = 38°$. The calculated moment of inertia of $\mathcal{J}^{(2)} = 6.5\ \hbar^2$/MeV is too small to support an extended regular rotational sequence, which reflects the proximity of the $N = 82$ shell closure and the suppression of the proton angular momentum by the pair correlations. We assign the three states of band L6 to this

configuration, which is used as reference for configurations that rotate about the long axis. The reference functions $E'_{L6}(\omega)$ and $J_{L6}(\omega)$ are generated analogous to the reference for rotation about the short axis, by replacing L6 for L1. The straight-line fit to J_{L6} has a slope of $\mathcal{J}^{(2)} = 8\hbar^2$/MeV, which compares well with the TAC value. Because of the small collectivity of rotation about the long axis, other configurations are not expected to support extended regular rotational bands; rather they may show up as sequences with roughly constant transition energies (tidal waves; cf. [30]). The sequences N1, L7, and L8 are of this kind. They may correspond to the configurations indicated in Table II. The other configurations with the correct parity and signature are alternatives. An unambiguous assignment is not possible. The configurations in Table II generated by the excitation of neutrons from the (E, F) into the (G, H) orbitals require around 2 MeV, which is too high (see in Fig. 8) to qualify for bands L7 and L8. Possible alternative configurations for bands L7 and L8 can involve the excitation of one or two protons from (E, F) into (G, H, I) coupled to the neutron S configuration, as in the case of band L2, which involves one- or two-proton excitation coupled to the proton S configuration. Such configurations will be considered in Sec. IV B2. However, it also seems possible that band L7 is the one-phonon wobbling excitation built on the neutron S configuration, which will be discussed in Sec. IV B3.

Figure 11 shows that the unpaired calculations fairly well reproduce the relative alignments of the different bands, which were used to make the configuration assignments. The experimental alignments are shifted upward by about $2\hbar$. Such a shift can be attributed to residual dynamic pair correlations, which reduce the angular momentum of the proton S-band L1 (reference) more strongly than in the other bands (cf. Sec. IV B2). This kind of modification has been discussed in Ref. [31]. The calculated Routhians cross around $\hbar\omega = 0.2$ MeV while with the experimental ones they cross around 0.45 MeV. Again, this is to be attributed to the neglected correlations in our extremely simplifying CSM interpretation. In particular, dynamic pair correlations, but also shape polarization, may be responsible for the energy shifts. As will be demonstrated in a forthcoming publication, one may derive experimental single-particle Routhians from the neighboring odd-Z isotones, which place the crossing at the right frequency [32].

One should note that bands with even spin and negative parity such as band N2 were also observed in neighboring nuclei such as ^{136}Nd [33] and ^{136}Ce [34], being interpreted as proton $\pi(dg)^1h^1$ and $\nu(sd)^1h^1$, respectively. The more collective behavior of the bands in ^{136}Nd allowed their observation up to high spins after two band crossings, whereas the bands in ^{136}Ce are very similar to those observed in ^{138}Nd. They were interpreted as rotational bands of a nucleus with nearly axial shape around a principal axis of the intrinsic reference system. We adopt the two-proton $\pi B^{-1}H$ configuration for band N2, which is similar to that assigned to the low-lying even-spin negative-parity band of ^{136}Nd.

Band N4 mainly decays to the ground-state band, and it has weak connecting transitions to the other negative-parity bands. It is interpreted as the $\pi E^{-1}\bar{A}$ configuration. This interpretation is in agreement with the feeding and

depopulation pattern of the band, which is mainly fed at the 9^- state from band L1 through the strong 454-keV $E1$ transition. This can be explained by a simple quasiproton excitation from the $\pi(dg)$ orbitals active in band N4 to the πh orbital active in band L1. The $E1$ transitions from band N4 to the g band, whose states are dominated by the $\pi(dg)$ configuration, can also be explained by a de-excitation from the πh orbital active in band N4 to the $\pi(dg)$ orbitals active in the g band. Another feature supporting the interpretation of band N4 as based on the $\pi E^{-1}\bar{A}$ configuration is that band D1, which is assigned to the $\pi F^{-1}\bar{A} \otimes \nu 10$ configuration (see below), decays only to the 13^- and 15^- states of band N4 and not to the other negative-parity bands. Furthermore, the two 9^- states of bands N1 and N4 have energies of 3239 and 3247 keV, respectively. Despite the very small energy difference of only 8 keV the two states do not interact. This supports the assignment of very different configurations to bands N1 and N4, with band N1 built on the $\nu B^{-1}H$ configuration and band N4 built on the $\pi E^{-1}\bar{A}$ configuration.

The 8^- state at 2980 keV is weakly populated by the 577- and 391-keV transitions from bands N2 and N3, respectively. This can be explained by a $\pi F^{-1}\bar{A}$ proton configuration and would complete the set of four two-quasiparticle negative-parity bands based on proton configurations with even and odd spins, as also predicted by the calculations shown in Fig. 11.

The assignment of the πh^2 configuration ($\pi 10$) to band L1 is also based on systematics and interacting boson model calculations [21]. As one can see in Figs. 12 and 13, which show the experimental excitation energy relative to a rotating liquid drop reference [36], the average slope of band L1 is smaller than that of the g band, suggesting a larger moment of inertia for band L1. This is in agreement with the results of the

FIG. 13. (Color online) The same as in Fig. 12 for the low- and medium-spin positive-parity bands.

TRS calculations, which show a triaxial shape with $\varepsilon_2 = 0.17$ and $\gamma = +30°$ for the assigned πh^2 configuration [21].

2. Paired CSM calculations

The CSM calculations in the preceding sections, in which zero pairing was assumed, provide an understanding of the global features of the band structure. As discussed there, some deviations from the observed data remain. Here the $\Delta I = 2$ positive-parity bands are compared with quasiparticle configurations calculated by means of the CSM with finite pairing [22,35], in order to assert the consequences of residual pair correlations.

For the bands L1–L5 we repeated the calculations, adopting the same deformation parameters $\varepsilon_2 = 0.17$ and $\gamma = +30°$
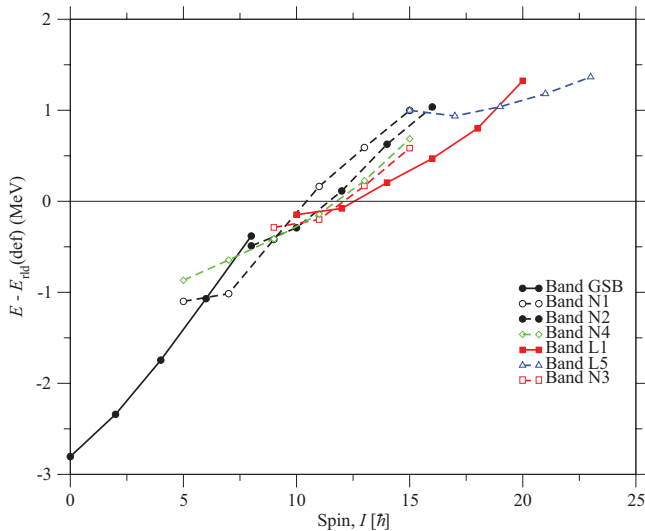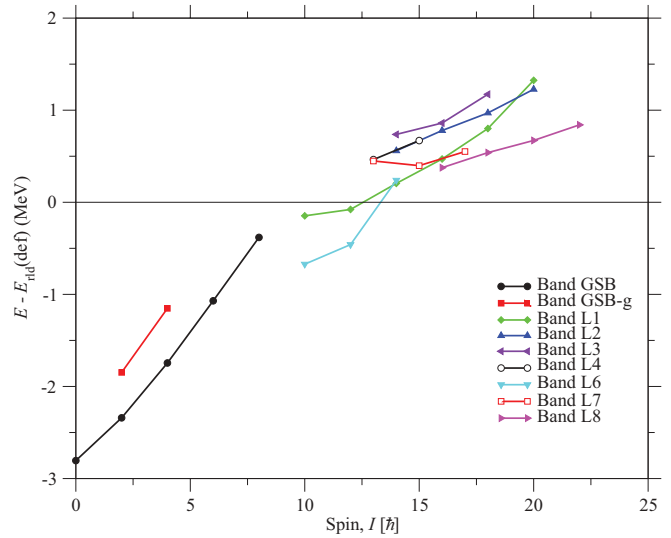

FIG. 12. (Color online) Experimental excitation energy relative to a rotating liquid drop reference for the negative-parity bands, the ground-state band, and the L1 band in ^{138}Nd. Solid and dashed lines are used for positive- and negative-parity configurations, respectively. Closed symbols are used for signature $\alpha = 0$ and open symbols for signature $\alpha = 1$.
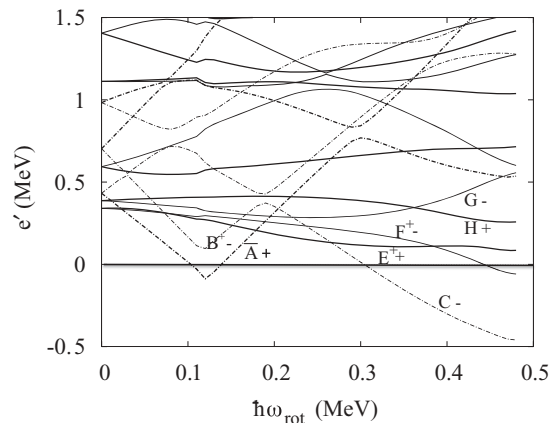

FIG. 14. Proton Routhians as functions of rotational frequency for ^{138}Nd, calculated using the constant mean-field parameters $\varepsilon_2 = 0.17$, $\gamma = +30°$, and $\Delta_p = 0.3$ MeV. The chemical potential is adjusted at each rotational frequency so that the quasiparticle vacuum has the correct particle number. This causes a small irregularity at the crossing at $\hbar\omega_{rot} = 0.12$ MeV. Positive- and negative-parity states are drawn by solid and dot-dashed curves, respectively.

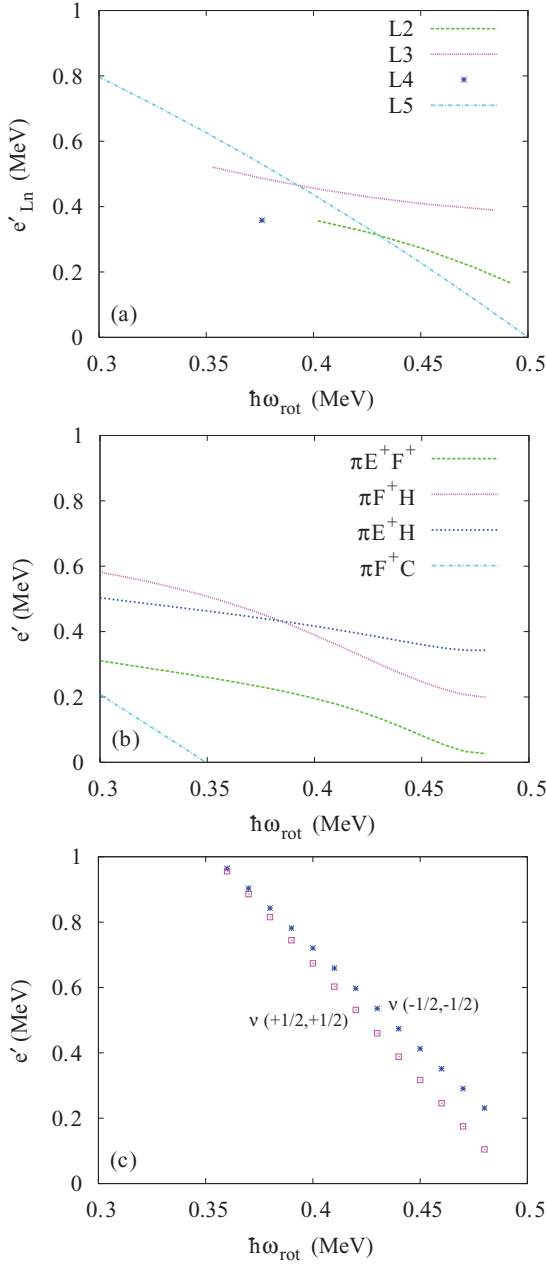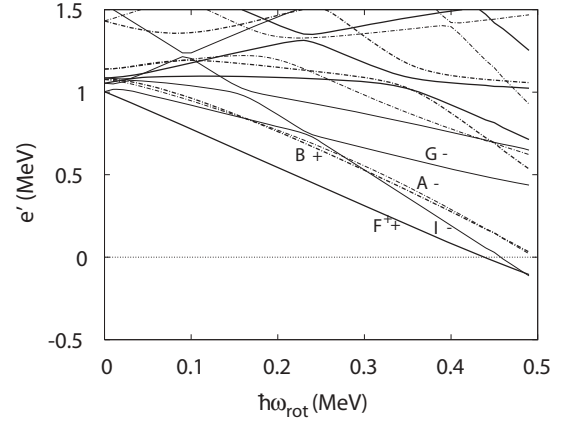FIG. 16. Proton Routhians as functions of rotational frequency for ^{138}Nd, calculated using the constant mean-field parameters $\epsilon_2 = 0.17$, $\gamma = -90°$, and $\Delta_p = 1.0$ MeV. The chemical potential is adjusted at each rotational frequency so that the quasiparticle vacuum has the correct particle number. Positive- and negative-parity states are drawn by solid and dot-dashed curves, respectively.

FIG. 15. (Color online) (a) Experimental Routhians of bands L2–L5 relative to that of band L1. (b) and (c) Energy difference between the different calculated (two-quasiparticle $\otimes \pi 10$) configurations and the $\pi 10$ configuration assigned to band L1. The calculations are performed at constant mean-field parameters $\varepsilon_2 = 0.17$, $\gamma = +30°$, and $\Delta_p = 0.3$ MeV.

represent relative alignments. Figure 15(b) shows the results of the calculation.

The lowest even-spin, positive-parity configuration $\pi E^\dagger F^\dagger$ can be assigned to band L2. This quasiparticle configuration, which does not have a particle-hole limit, is an alternative to the $\pi F^{-1}H$ assignment resulting from the zero-pairing calculations. The second lowest even-spin, positive-parity configuration $\pi F^\dagger H$ can then be assigned to band L3. The third low-lying even-spin, even-parity configuration is $\pi E^\dagger G$. It is not shown, because we could not associate it with one of the experimental bands. In Sec. IV B 1, its zero-pairing counterpart $\pi E^{-1}G$ has been assigned to band L3. The lowest odd-spin configuration in Fig. 15(b) is $\pi E^\dagger H$, which becomes $\pi E^{-1}H$ in the zero-pairing limit. It is assigned to band L4, for which only one transition was observed. The configuration $\pi F^\dagger C$ can be assigned to band L5, like $\pi F^{-1}C$ in the zero-pairing limit (see Secs. IV A and IV B 1).

The calculations with finite pairing reproduce the experimental slope of the relative Routhians (relative alignment) better than the zero-pairing calculations. However, they place the relative Routhians too low as compared with the experiment. This is particularly severe for the configuration $\pi F^\dagger C$, which has a lower Routhian than the reference configuration $\pi 10$ for $\hbar\omega > 0.3$ MeV. The comparison of the zero- and finite-pairing calculations with experiment seems to indicate that the static pair correlations are in fact quenched but that there are still dynamic pair correlation present (cf. discussion in Sec. IV B 1).

Next we discuss bands L7 and L8, which decay to L6. The CSM calculations are carried out with the deformation parameters $\varepsilon_2 = 0.17$ and $\gamma = -90°$ (long axis) and the pairing strengths $\Delta_n = 0.3$ MeV and $\Delta_p = 1.0$ MeV. As already discussed, the TAC calculations with these parameters show that configurations containing $\nu h^2\nu 0 = \nu 10$ prefer rotation about the long axis with a moment of inertia that is too small to support a regular rotational band extended over several spins. Band L6, defined as the 14^+–12^+–10^+ sequence, is
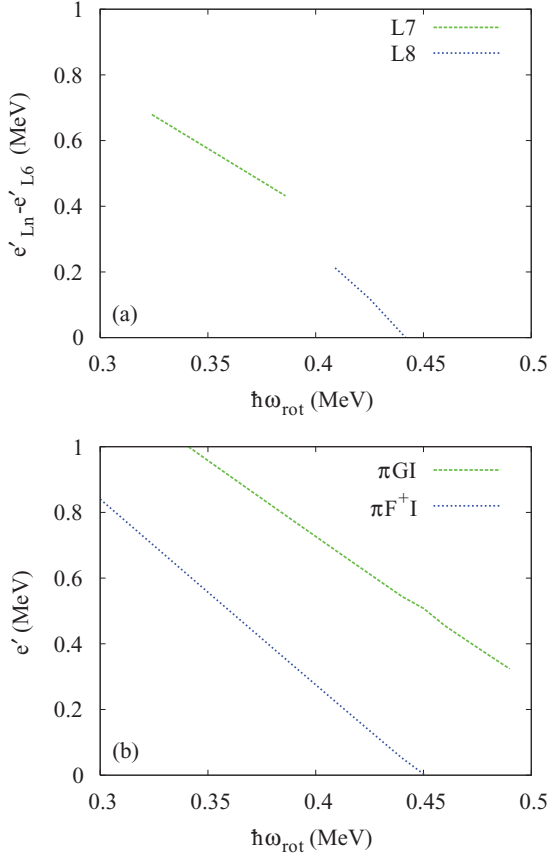
(short axis) and pairing parameters $\Delta_n = 1.0$ MeV and $\Delta_p = 0.3$ MeV, whereas chemical potentials were adjusted at each rotational frequency such that the quasiparticle vacuum has the correct particle number. As seen in Fig. 14, the proton S configuration $\pi h^2\pi 0\nu 0 = \pi 10\nu 0$ becomes yrast at $\hbar\omega_{rot} = 0.12$ MeV. As for the zero-pairing calculations, we examine two-quasiparticle excitations relative to this configuration. Figure 15(a), extracted from Fig. 11, shows the experimental Routhians e' of bands L2–L5 relative to band L1. Their slopes
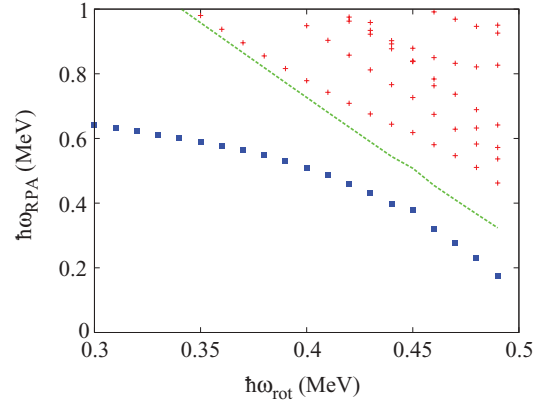
FIG. 18. (Color online) Calculated excitation energies of the RPA solutions built on the aligned $\nu 10$ configuration as functions of the rotational frequency in ^{138}Nd. Among them, the collective solution is emphasized by blue squares. Note that noncollective solutions are occasionally overlooked in the present algorithm, which however does not have any consequences for the discussion. The green dotted curve is the unperturbed πGI state.

based on this two-quasiparticle configuration. The residual interaction between quasiparticles is taken as the quadrupole-quadrupole force.

The RPA equation for odd-spin excitations can be cast into the form

$$\omega^2 = \omega_{\text{rot}}^2 \frac{\left[\mathcal{J}_x - \mathcal{J}_y^{(\text{eff})}(\omega)\right]\left[\mathcal{J}_x - \mathcal{J}_z^{(\text{eff})}(\omega)\right]}{\mathcal{J}_y^{(\text{eff})}(\omega)\mathcal{J}_z^{(\text{eff})}(\omega)}, \qquad (6)$$

which is particularly suited for the description of the wobbling mode [37]. However, it is noted that these equations also have noncollective solutions. Here, $\mathcal{J}_x$ is the usual kinematic moment of inertia including the contribution from the aligned quasiparticle(s), whereas $\mathcal{J}_{y,z}^{(\text{eff})}(\omega)$ are calculated self-consistently for a given value of ω.

Figure 18 shows almost all solutions located lower than 1 MeV. We will focus on the two lowest solutions among them. The character of the solutions must be judged as follows: First of all, the collective solutions are located at low energies, being well separated from other noncollective ones in ideal cases. Second, their wave functions are distributed over many two-quasiparticle states in a way which enhances certain transition amplitudes, such as in the case of the γ vibration mode, in which the $K = 2$ transition amplitudes are dominant. In the case of the present lowest solution, the $K = 1$ and 2 transition amplitudes are strong and fully mixed with a definite phase relation, which would lead to a characteristic staggering of $B(E2)$ [39]. Further information that signals the wobbling character of the solution is obtained from the calculated three moments of inertia [cf. Fig. 19(a)] and the calculated wobbling angles [38] [cf. Fig. 19(b)]. In particular, the calculated moments of inertia can be understood by assuming an irrotational-like γ dependence ($\mathcal{J}_x < \mathcal{J}_z$) superimposed by the contribution to $\mathcal{J}_x$ from the aligned νh^2 pair. This makes $\mathcal{J}_x > \mathcal{J}_z$, as in the celebrated case of ^{163}Lu, where a $\pi i_{13/2}$ orbital makes $\mathcal{J}_x > \mathcal{J}_y$ [6,39]. Thus we propose to interpret the observed band L7 as a wobbling mode, although its vacuum is not a well-deformed state.
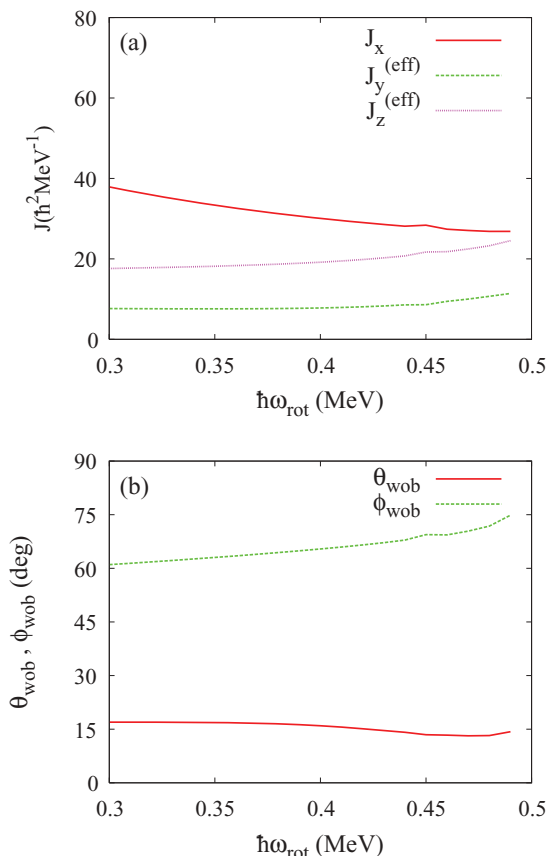
FIG. 17. (Color online) (a) Experimental Routhians of bands L7 and L8 relative to that of band L6. (b) Energy difference between the different calculated (two-quasiparticle $\otimes \nu 10$) configurations and the $\nu 10$ configuration assigned to band L6. The calculations are performed at constant mean-field parameters $\varepsilon_2 = 0.17$, $\gamma = -90°$, and $\Delta_p = 1.0$ MeV.

assigned to the configuration $\pi 0\nu h^2 \nu 0 = \pi 0\nu 10$. We use it as the reference configuration for rotation about the long axis. We adopted the following set of reference parameters: $e' = -0.085$ MeV and $i_x = 10.259\hbar$ at $\hbar\omega = 0.324$ MeV, $\mathcal{J}^{(0)} = 3\hbar^2/$MeV, and $\mathcal{J}^{(2)} = 8\hbar^4/$MeV^3.

Here and further in this paragraph the proton configurations are taken relative to the g vacuum. Figure 16 indicates that the lowest even-spin excitation is $\pi F^\dagger I \otimes \nu 10$. As seen in Fig. 17, it can be assigned to the observed band L8. In contrast, the observed odd-spin band L7 cannot be associated with any calculated two-quasiparticle excitation. Figure 17(b) shows that the lowest odd-spin configuration $\pi GI \otimes \nu 10$ is calculated at a much higher excitation energy than the lowest even-spin $\pi F^\dagger I \otimes \nu 10$ configuration. This is in disagreement with the experimental bands L7 and L8 shown in Fig. 17(a), the Routhians of which almost continue each other.

3. Random-phase approximation calculations for wobbling

As an alternative, band L7 can be interpreted as a collective wobbling excitations built on the νh^2 configuration. We have performed random-phase approximation (RPA) calculations

FIG. 19. (Color online) (a) Calculated moments of inertia and (b) wobbling angles as functions of the rotational frequency in ^{138}Nd.

In the frequency range in which the lowest solution is collective, the second lowest solution is almost purely the two-quasiparticle state πGI, whose Routhian is shown by the green dotted curve. As ω increases, the πGI component in the RPA wave function moves gradually from the second to the lowest solution, and eventually the lowest solution becomes unstable.

In general, the instability of a collective mode leads to a "phase transition" of the mean field to a lower symmetry. In the case of the wobbling mode around a principal axis, the corresponding new mean field is a tilted-axis rotating state [38]. Rotation about a tilted axis is expected to be observed as a $\Delta I = 1$ dipole band [23], as will be discussed in the next section. In the present case the instability is triggered by the steep lowering of the lowest πGI two-quasiparticle state. The tilted-axis state appearing after this instability is expected to contain νh^2 and one or two $\pi(dg)$. The calculated frequency of the instability, $\hbar\omega_{rot} \sim 0.5$ MeV, is larger than the frequency of the highest transition observed in band L7, $\hbar\omega_{rot} = 0.386$ MeV.

Interpreting band L7 as the one-phonon excitation, one is tempted to assign L8 to the two-phonon excitation, because it has even spin. However Fig. 17(a) indicates that the frequency ranges of L7 and L8 are displaced from each other and that L8 is lower than L7 when the bands are extrapolated to a common frequency.

Finally, an interesting feature of the level scheme above the 10^+ isomer is the existence of three excited states with spins 11^+, 12^-, and 13^- which are strongly populated from

the decay of the dipole band D1. We did not observe collective cascades built on these states, which suggests that they are of single-particle nature. An 11^+ state can be constructed by exciting two more quasineutrons into $(s_{1/2})_{1^+}$, which generates a maximal aligned spin of $11\hbar$. The 12^- and 13^- states can be explained by four-quasiparticle configurations with two protons in $(d_{5/2}g_{7/2})_{6^+}$ coupled to two neutrons in $(h_{11/2}s_{1/2})_{6^-}$ or $(h_{11/2}d_{3/2})_{7^-}$, respectively. Such configurations would explain the strong connecting transitions among the 11^+, 12^-, and 13^- states. They would also account for the strong population from the 13^- state of band D1, for which a $\pi h^1(dg)^1 \otimes \nu h^2$ configuration is assigned (see below). Negative-parity states 12^- and 13^- were also observed in ^{140}Nd, where they are populated by the de-excitation of the 20^+ six-quasiparticle isomer [40]. In Ref. [40] the configuration $\pi(dg)^4 \otimes \nu h^2$ was assigned to the isomer, and the 12^- and 13^- states were interpreted as the aligned configurations $\pi(dg)^2 \otimes \nu h^1(sd)^1$.

C. The $\Delta I = 1$ bands

The experimental Routhians and alignments of bands D1–D8 relative to band L1 are shown in Fig. 20. Figure 21 displays the corresponding calculated quantities relative to the $\pi 10 = \pi ABEF$ configuration. The large number of dipole bands originates from the combination of $h_{11/2}$ protons, which align with the short axis, and $h_{11/2}$ neutrons, which align with the long axis. As a compromise, the rotational axis lies in the short-long principal plane, being tilted away from the principal axes by a large angle. The tilt breaks the $\mathcal{R}_x(\pi)$ symmetry that induces the signature quantum number, and one observes a $\Delta I = 1$ sequence of rotational states, i.e., a dipole band [5]. The rotational mode is predominantly of magnetic nature, because the mutually perpendicular angular momenta of the proton and neutron $h_{11/2}$ orbitals combine to a large transverse magnetic moment, which generates strong $M1$ transitions.

Most of the dipole bands result from changing the neutron configuration of the various proton configurations in Table II from $\nu 0$ to $\nu 10$, which contains the two $h_{11/2}$ neutron holes that align their angular momentum with the long axis. Table III lists the configurations that originate from these combinations and suggests how to interpret the observed dipole bands. Figure 22 shows that the $B(M1)$ values of these bands are large, reflecting the long angular momentum vectors of the $h_{11/2}$ particles, which enclose a large angle with the rotational axis. It should be noted that the $B(M1)$ values are calculated, not measured. The $B(M1)$ values change only weakly with the angular frequency, not showing the decrease that is characteristic for pure magnetic rotation [41]. The reason is that the deformation is still substantial. Hence the rotational mode has an intermediate character, being in between magnetic and collective electric rotation [41]. The ratios $B(M1)/B(E2) > 50 \ \mu_N^2/(e\,b)^2$. For many bands they are larger than 1000 $\mu_N^2/(e\,b)^2$. This explains the absence of any $E2$ crossover transitions in all dipole bands observed in this experiment, with the only exception of band D1, for which $B(M1)/B(E2) \sim 30 \ \mu_N^2/(e\,b)^2$.

The configuration assigned to band D1, $\pi F^{-1}\bar{A} \otimes \nu 10$, is supported by the comparison with the odd-even ^{139}Nd
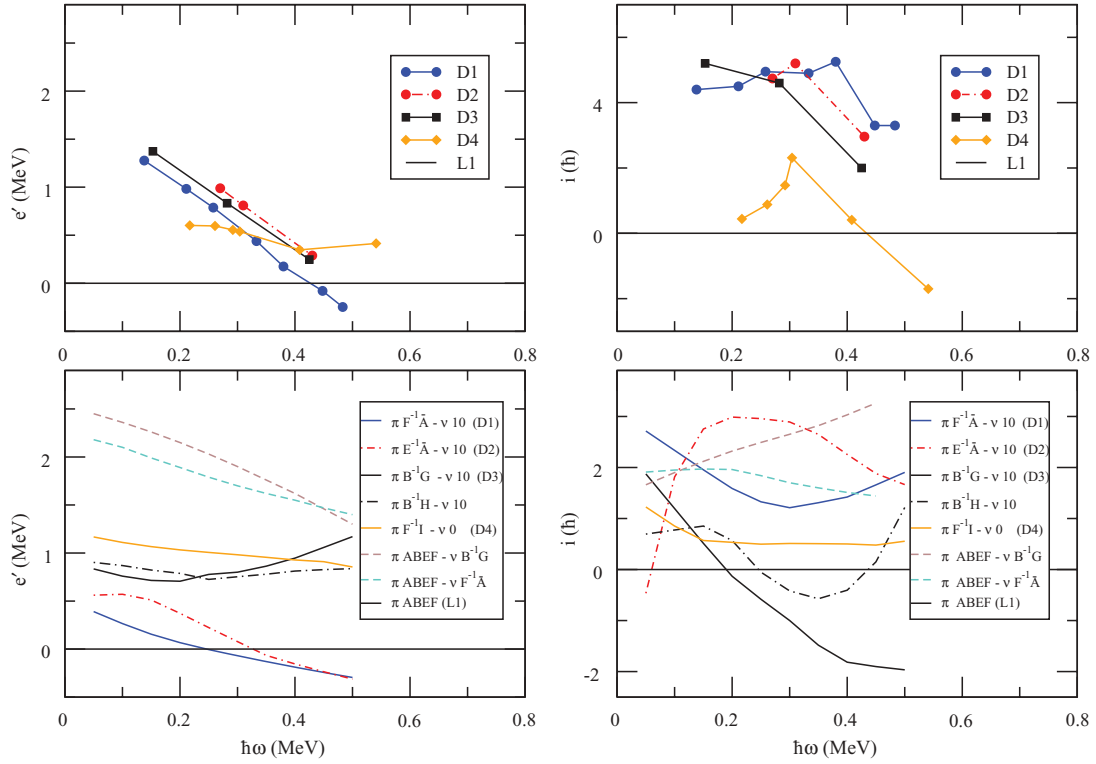
FIG. 20. (Color online) Experimental and calculated Routhians and single-particle alignments relative to band L1 for the $\Delta I = 1$ bands D1–D4 of ^{138}Nd. The line type indicates the parity: full ($\pi = +$) or dash-dotted ($\pi = -$). All calculated Routhians, except $\pi ABEI\nu 0$, are shifted by $E_{exp,L6}(10^+) - [E_{calc,\nu 10}(\omega = 0) - E_{calc,\nu 0}(\omega = 0)]$ in order to account for the energy needed for breaking a neutron pair.
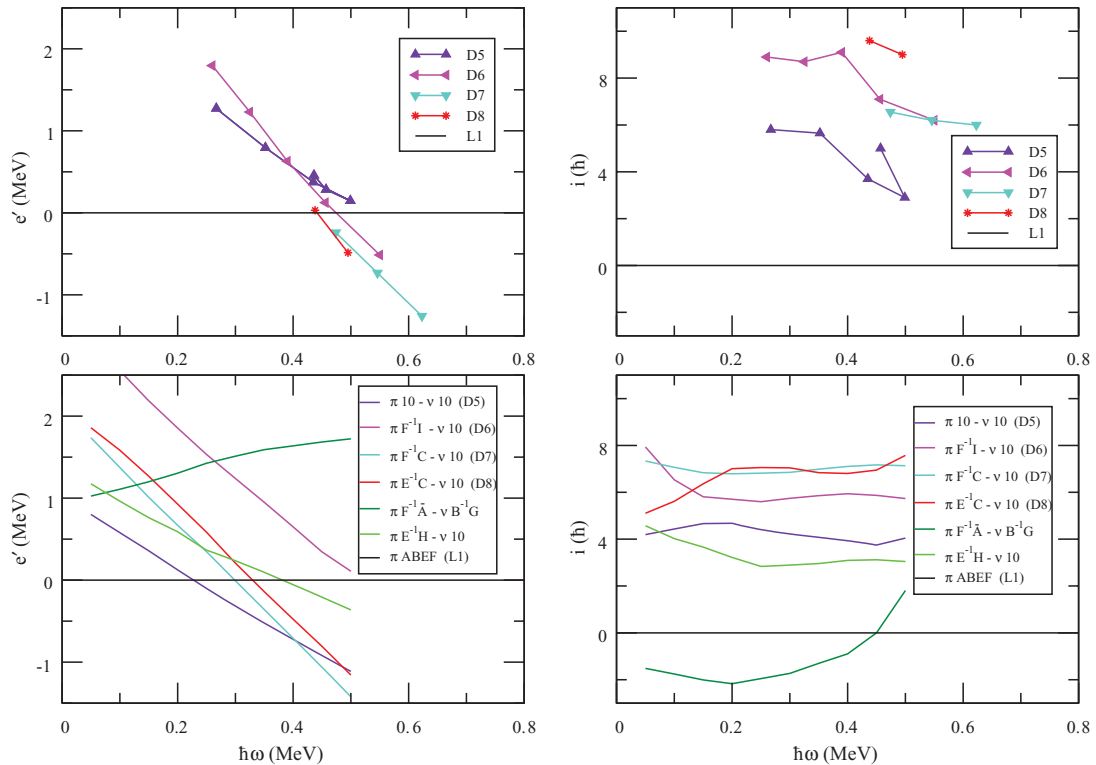

FIG. 21. (Color online) Experimental and calculated Routhians and single-particle alignments relative to band L1 for the $\Delta I = 1$ bands D5–D8 of ^{138}Nd. The line type indicates the parity: full ($\pi = +$) or dash-dotted ($\pi = -$). All calculated Routhians, except $\pi ABEI\nu 0$, are shifted by $E_{exp,L6}(10^+) - [E_{calc,\nu 10}(\omega = 0) - E_{calc,\nu 0}(\omega = 0)]$ in order to account for the energy needed for breaking a neutron pair.

TABLE III. Single-particle configurations for the $\Delta I = 1$ bands of ^{138}Nd.

Configuration	π	bands
$\pi 10 \otimes \nu 10$	$+$	D5
$\pi B^{-1}G \otimes \nu 10$	$-$	D3
$\pi B^{-1}H \otimes \nu 10$	$-$	
$\pi E^{-1}\bar{A} \otimes \nu 10$	$-$	D2
$\pi F^{-1}\bar{A} \otimes \nu 10$	$-$	D1
$\pi F^{-1}C \otimes \nu 10$	$-$	D7
$\pi E^{-1}C \otimes \nu 10$	$-$	D8
$\pi E^{-1}G \otimes \nu 10$	$+$	
$\pi E^{-1}H \otimes \nu 10$	$+$	
$\pi F^{-1}G \otimes \nu 10$	$+$	
$\pi F^{-1}H \otimes \nu 10$	$+$	
$\pi F^{-1}\bar{A} \otimes \nu B^{-1}G$	$+$	
$\pi B^{-1}C \otimes \nu 10$	$+$	
$\pi F^{-1}I \otimes \nu 0$	$+$	D4
$\pi F^{-1}I \otimes \nu 10$	$+$	D6

neighboring nucleus, in which a three-quasiparticle band has been observed at an excitation energy relative to the 10^+ isomer which is similar to that of band D1 (see Fig. 23). The configuration assigned to the band in ^{139}Nd is $\pi h^1 (dg)^1 \otimes \nu h^1$ [13,42]. Such a dipole band was also observed in the neighboring isotone ^{136}Ce [34] and interpreted as the configuration $\pi h^1 (dg)^1 \otimes \nu h^2$ rotating around a tilted axis. The measured transition probabilities support the interpretation of the band in ^{136}Ce as "magnetic rotation." The similarity of the two corresponding dipole bands in ^{139}Nd and ^{136}Ce and band D1 of ^{138}Nd strongly supports the $\pi F^{-1}\bar{A} \otimes \nu 10$ [$\pi h^1 (dg)^1 \otimes \nu h^2$] configuration for band D1, which is in disagreement with the $\pi h^2 \otimes \nu h^2$ configuration proposed in Ref. [21].

The TAC calculation for the configuration $\pi F^{-1}\bar{A} \otimes \nu 10$ gave a shallow minimum outside the short-long principal plane at $\phi \approx 30°$, which indicates instability with respect to intrinsic chirality around $\hbar\omega \approx 0.35$ MeV. Indeed, band D2 decays through dipole transitions to band D1 and is nearly parallel to
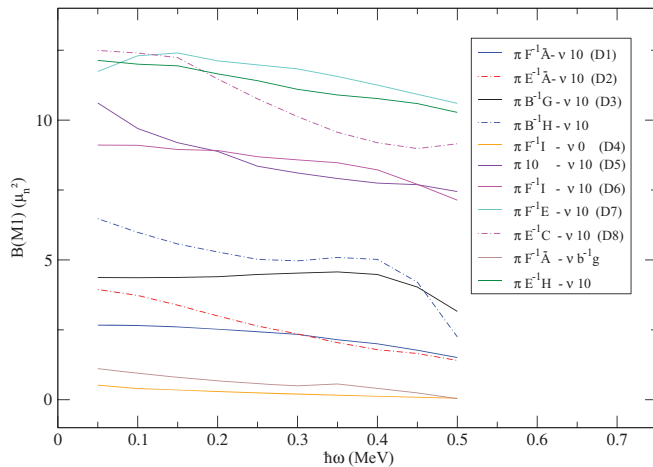
FIG. 22. (Color online) Calculated $B(M1)$ for the configurations assigned to the dipole bands of ^{138}Nd.

it. This is characteristic for chiral bands, and band D2 could be the first candidate in an even-even nucleus. The observation of chiral partner bands claimed in the neighboring ^{136}Nd nucleus [43] were not confirmed by either lifetime measurements or calculations [44]. However, one cannot exclude the alternative interpretation for band D2, as a particle-hole configuration closely related to band D1. One possibility is the excitation of two protons from E to F, giving rise to the $\pi E^{-1}\bar{A} \otimes \nu 10$ configuration.

Band D3 is built on the $14^{(-)}$ state and decays to negative-parity nonyrast states, which in turn decay to the 10^+ isomer with $\nu 10$ configuration. A possible configuration which accounts for its decay pattern is $\pi B^{-1}G \otimes \nu 10$.

Band D4 is the lowest-lying dipole band. It is built on the 10^+ state and decays to band L1 and to the ground-state band. Its alignment of $i < 2\hbar$ relative to the reference is too low to involve two $h_{11/2}$ protons and two $h_{11/2}$ neutron holes. There are two possibilities for generating positive parity and low alignment: (i) One may combine the negative-parity proton configurations listed in Table II with the negative-parity neutron configurations listed in the same table. One example is $\pi F^{-1}\bar{A} \otimes \nu B^{-1}G$, which is included in Table III and Fig. 20. (The other combinations, which look similar, are left out for clarity.) This type has $B(M1)/B(E2) > 300~\mu_N^2/(e\,b)^2$. (ii) The pure proton excitation $\pi F^{-1}I \otimes \nu 0$ has a smaller ratio of $B(M1)/B(E2) \approx 4\mu_N^2/(e\,b)^2$. We tentatively adopt the $\pi F^{-1}I \otimes \nu 0$ assignment, because the calculated alignment and Routhian correlate better with experiment, and the assignment is consistent with the interpretation of D6, which decays into D4, as generated by the alignment of the two $h_{11/2}$ neutrons. However, the nonobservation of crossover quadrupole transitions in band D4 put a limit of the $B(M1)/B(E2) > 500~\mu_N^2/(e\,b)^2$, which speaks in favor of the $\pi F^{-1}\bar{A} \otimes \nu B^{-1}G$ configuration.

Band D5 is built on the $16^{(+)}$ state and decays to band D4. We assign it to the configuration $\pi 10 \otimes \nu 10$, because both the Routhian and the aligned angular momentum are in agreement with experiment.

Band D6 is built on the $19^{(+)}$ state and decays to band L8 whose configuration is $\nu E^{-1}G$ and to band L3 whose configuration is $\pi E^{-1}G$. The configurations $\pi F^{-1}I \otimes \nu 10$ and $\pi E^{-1}H \otimes \nu 10$, shown in Fig. 21, are possible candidates. The positive-parity configuration $\pi F^{-1}\bar{A} \otimes \nu B^{-1}G$ can be excluded because its Routhian behaves completely differently, and the aligned angular momentum is too low. None of the configurations $\pi F^{-1}I \otimes \nu 10$ and $\pi E^{-1}H \otimes \nu 10$ fit well with band D6. The Routhian of $\pi F^{-1}I \otimes \nu 10$ is too high, and $\pi E^{-1}H \otimes \nu 10$ has too low an alignment. Based on the better agreement of the aligned angular momentum we prefer the $\pi F^{-1}I \otimes \nu 10$ assignment.

The two bands D7 and D8 are observed above spin $22^{(-)}$ and feed the top level of band D1. They may correspond to the six-quasiparticle configurations $\pi F^{-1}C \otimes \nu 10$ and $\pi E^{-1}C \otimes \nu 10$, respectively.

V. CONFIGURATION ASSIGNMENTS

The configuration assignments to the low- and medium-spin states are summarized in Table IV.
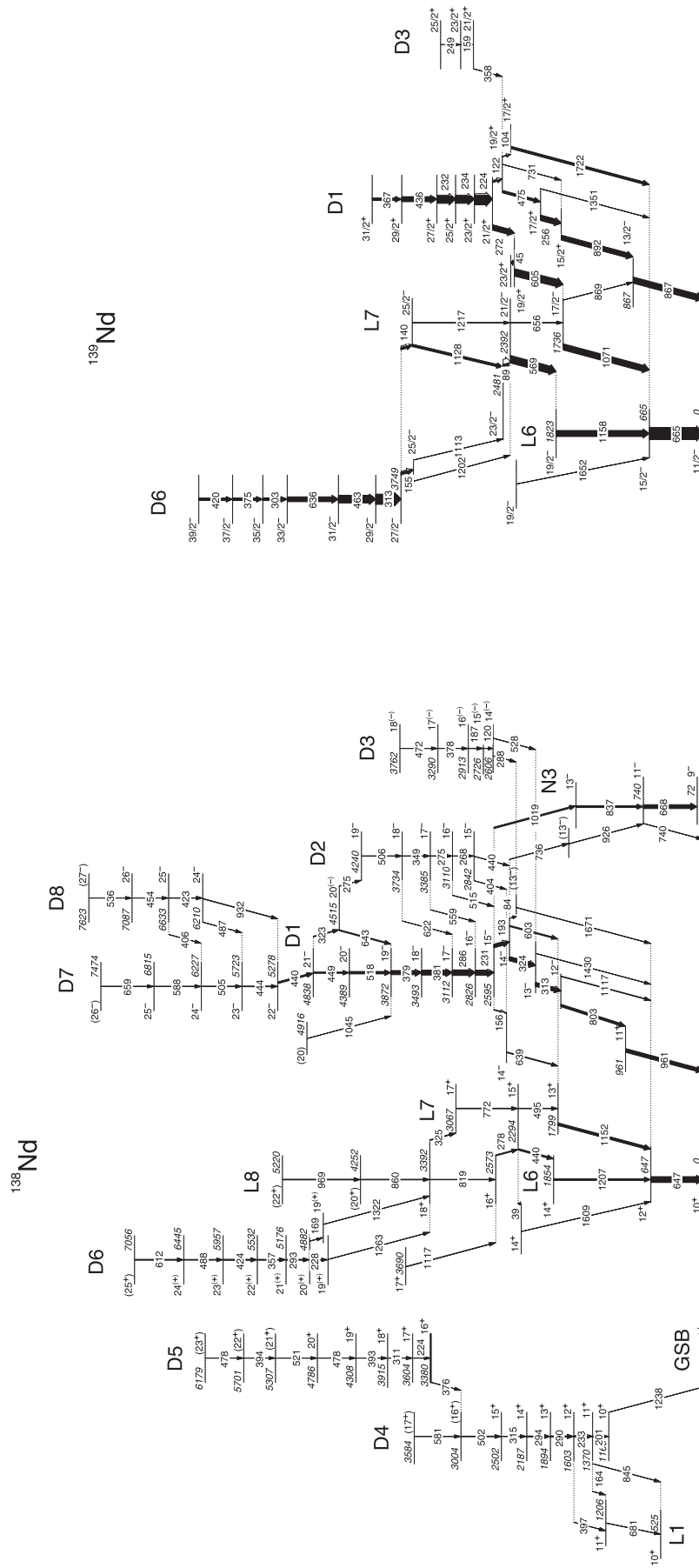
FIG. 23. Comparison between the partial level scheme of ^{138}Nd and ^{139}Nd showing the similarity of the level structure above the 10^+ isomer.

TABLE IV. Configuration assignments to the low- and medium-spin bands of ^{138}Nd in terms of particle-hole excitations with respect to the $\pi ABEF = \pi 10$ reference configuration assigned to band L1 or the corresponding quasiproton vacuum for small finite pairing. The rotation axis is also indicated, which can be tilted (TAC) or parallel to a principal axis (PAC) of the intrinsic reference system of the nucleus. In the case of PAC, l and s indicate the long and short axes, respectively.

Band	Intensity (%)	Configuration	Rotation type	States	Comments
g band	100	$\pi 0 \otimes \nu 0$		$2^+ - 8^+$	
γ band		γ band		$2^+ - 4^+$	Decays to g band
N1	39	$\pi 0 \otimes \nu B^{-1} H \nu 10$	PAC-l	$5_1^- - 15^-$	Decays to g band
N2	14	$\pi B^{-1} H \pi 10 \otimes \nu 0$	PAC-s	$8_2^- - 16^-$	Decays to N1, N3, 8_1^-
N3	2	$\pi B^{-1} G \pi 10 \otimes \nu 0$	PAC-s	$9_2^- - 15^-$	Decays to N2, N4, 8_1^-
N4	89	$\pi E^{-1} \bar{A} \pi 10 \otimes \nu 0$	PAC-s	$7_2^- - 15^-$	Decays to N1, N3, GSB
8_1^-	17	$\pi F^{-1} \bar{A} \pi 10 \otimes \nu 0$	PAC-s	$8_1^-, 8_2^-$	Decays to N1
L1	64	$\pi 10 \otimes \nu 0$	PAC-s	$10^+ - 20^+$	Decays to N2, N3
L2	6	$\pi F^{-1} H \pi 10 \otimes \nu 0$ or $\pi E^{\dagger} F^{\dagger} \pi 10 \otimes \nu 0$	PAC-s	$14^+, 16^+, 18^+$	Decays to L1
L3	2	$\pi E^{-1} G \pi 10 \otimes \nu 0$ or $\pi F^{\dagger} H \pi 10 \otimes \nu 0$	PAC-s	$14^+ - 20^+$	Decays to L1, L4
L4	2	$\pi E^{-1} H \pi 10 \otimes \nu 0$	PAC-s	$13^+, 15^+$	Decays to L1, L3
L5	8	$\pi F^{-1} C \pi 10 \otimes \nu 0$ or $\pi 10 \otimes \nu h^2$	PAC-s	$15^{(-)} - 23^{(-)}$	Decays to L1, D4
L6	24	$\pi 0 \otimes \nu 10$	PAC-l	$10^+ - 14^+$	Band head is isomeric
L7	11	wobbling or $\pi 0 \otimes \nu F^{-1} G \nu 10$ or $\pi G I \pi 0 \otimes \nu 10$	PAC-l	$13^+ - 17^+$	Decays to L6
L8	2	$\pi 0 \otimes \nu E^{-1} G \nu 10$ or $\pi F^{\dagger} I \pi 0 \otimes \nu 10$	PAC-l	$16^+ - 22^+$	Decays to L7
D1	21	$\pi F^{-1} \bar{A} \pi 10 \otimes \nu 10$	TAC	$13^- - 21^-$	Decays to N4, L8
D2	2	$\pi E^{-1} \bar{A} \pi 10 \otimes \nu 10$ or chiral	TAC	$15^- - 19^-$	Decays to D1
D3	1	$\pi B^{-1} G \pi 10 \otimes \nu 10$	TAC	$14^- - 18^-$	Decays to nonyrast $\pi = -$
D4	5	$\pi F^{-1} I \pi 10 \otimes \nu 0$ or $\pi F^{-1} \bar{A} \otimes \nu b^{-1} g$	TAC	$10^+ - 17^+$	Decays to L1 and GSB
D5	1	$\pi 10 \otimes \nu 10$	TAC	$16^{(+)} - 23^{(+)}$	Decays to D4 and $\pi = -$
D6	4	$\pi F^{-1} I \pi 10 \otimes \nu 10$ or $\pi E^{-1} H \otimes \nu 10$	TAC	$19^{(+)} - (25^+)$	Decays to L7
D7	3	$\pi F^{-1} C \pi 10 \otimes \nu 10$	TAC	$22^{(-)} - (26^-)$	Decays to D1
D8	2	$\pi E^{-1} C \pi 10 \otimes \nu 10$	TAC	$24^{(-)} - (27^-)$	Decays to D7

VI. SUMMARY

High-spin states in ^{138}Nd have been populated in the reaction ^{94}Zr(^{48}Ca, 4n) at beam energies of 188 and 195 MeV. The GASP spectrometer was used to detect the γ-ray coincidences. A very rich and rather complete level scheme was constructed. Most of the existing information was confirmed. New bands were observed at low and medium spins (four negative-parity bands at low spins, eight bands of quadrupole transitions, and eight bands of dipole transitions at medium spins). The observed bands were discussed using the CSM, TAC and RPA approaches. The possible existence of a wobbling excitation was suggested, which would be the first in this mass region. Configuration assignments for the different bands were proposed that correspond to rotation either around a principal axis or a tilted axis of the intrinsic reference system

of one and the same nucleus. The orientation depends on the presence in the configurations of protons and neutrons in the $h_{11/2}$ orbitals. Two dipole bands have properties which are consistent with a dynamic chirality. They represent candidates for chiral partners in an even-even nucleus. The consistency of the configuration assignments to the observed bands strongly suggests the existence of a stable triaxial deformation at medium spin in this mass region.

[1] L. Wilets and M. Jean, Phys. Rev. **102**, 788 (1956).
[2] A. S. Davydov and A. A. Chaban, Nucl. Phys. **20**, 499 (1960); **8**, 237 (1958).
[3] A. Bohr and B. R. Mottelson, *Nuclear Structure* (Benjamin, Reading, MA, 1975), Vol. II.
[4] S. Frauendorf and J. Meng, Nucl. Phys. A **617**, 131 (1997).
[5] S. Frauendorf, Rev. Mod. Phys. **73**, 463 (2001).
[6] S. W. Ødegård *et al.*, Phys. Rev. Lett. **86**, 5866 (2001).
[7] C. M. Petrache, D. Bazzacco, S. Lunardi, C. Rossi Alvarez, G. de Angelis, M. De Poli, D. Bucurescu, C. A. Ur, P. B. Semmes, and R. Wyss, Nucl. Phys. A **597**, 106 (1996).
[8] S. Mukhopadhyay *et al.*, Phys. Rev. Lett. **99**, 172501 (2007).
[9] C. M. Petrache *et al.*, Phys. Lett. B **373**, 275 (1996).
[10] C. M. Petrache *et al.*, Nucl. Phys. A **617**, 228 (1997).
[11] C. M. Petrache *et al.*, Phys. Rev. C **61**, 011305(R) (1999).
[12] C. M. Petrache *et al.*, Phys. Rev. C **72**, 064318 (2005).
[13] S. Bhowal *et al.*, Phys. Rev. C **84**, 024313 (2011).
[14] S. Lunardi *et al.*, Phys. Rev. C **69**, 054302 (2004).
[15] A. Neußer *et al.*, Phys. Rev. C **70**, 064315 (2004).
[16] C. M. Petrache *et al.* (private communication).
[17] N. Yoshikawa, Nucl. Phys. A **243**, 143 (1974).

[18] J. Deslauriers, S. C. Gujrathi, and S. K. Mark, Z. Phys. A **303**, 151 (1981).

[19] M. Müller-Veggian, H. Beuscher, R. M. Lieder, Y. Gono, D. R. Haenni, A. Neskakis, and C. Mayer-Böricke, Z. Phys. A **290**, 43 (1979).

[20] M. Müller-Veggian, H. Beuscher, D. R. Haenni, R. M. Lieder, A. Neskakis, and C. Mayer-Böricke, Nucl. Phys. A **344**, 89 (1980).

[21] G. de Angelis *et al.*, Phys. Rev. C **49**, 2990 (1994).

[22] R. Bengtsson and S. Frauendorf, Nucl. Phys. A **327**, 139 (1979).

[23] S. Frauendorf, Nucl. Phys. A **557**, 250c (1993).

[24] S. Frauendorf, Nucl. Phys. A **677**, 115 (2000).

[25] T. Bengtsson and I. Ragnarsson, Nucl. Phys. A **436**, 14 (1985).

[26] I. Ragnarsson, Nucl. Phys. A **591**, 387 (1995).

[27] A. V. Afanasjev, D. B. Fossan, G. J. Lane, and I. Ragnarsson, Phys. Rep. **322**, 1 (1999).

[28] I. Ragnarsson, V. P. Janzen, D. B. Fossan, N. C. Schmeing, and R. Wadsworth, Phys. Rev. Lett. **74**, 3935 (1995).

[29] R. Bengtsson, S. Frauendorf, and F. R. May, At. Data Nucl. Data Tables **35**, 15 (1986).

[30] S. Frauendorf, Y. Gu, and J. Sun, Int. J. Mod. Phys. E **20**, 465 (2011).

[31] Y. R. Shimizu *et al.*, Rev. Mod. Phys. **61**, 131 (1989).

[32] S. Frauendorf and C. M. Petrache [Phys. Rev C (to be published)].

[33] C. M. Petrache *et al.*, Phys. Lett. B **373**, 275 (1996).

[34] S. Lakshmi, H. C. Jain, P. K. Joshi, Amita, P. Agarwal, A. K. Jain, and S. S. Malik, Phys. Rev. C **66**, 041303(R) (2002).

[35] M. Matsuzaki, Y. R. Shimizu, and K. Matsuyanagi, Phys. Rev. C **69**, 034325 (2004).

[36] B. G. Carlsson and I. Ragnarsson, Phys. Rev. C **74**, 011302(R) (2006).

[37] E. R. Marshalek, Nucl. Phys. A **331**, 429 (1979).

[38] M. Matsuzaki and S.-I. Ohtsubo, Phys. Rev. C **69**, 064317 (2004).

[39] M. Matsuzaki, Y. R. Shimizu, and K. Matsuyanagi, Phys. Rev. C **65**, 041303(R) (2002).

[40] C. M. Petrache *et al.*, Phys. Rev. C **74**, 034304 (2006).

[41] S. Frauendorf, Rev. Mod. Phys. **73**, 463 (2001).

[42] S. Kumar, R. Palit, H. C. Jain, I. Mazumdar, P. K. Joshi, S. Roy, A. Y. Deo, Z. Naik, S. S. Malik, and A. K. Jain, Phys. Rev. C **76**, 014306 (2007).

[43] E. Mergel *et al.*, Eur. Phys. J. A **15**, 417 (2002).

[44] S. Mukhopadhyay *et al.*, Phys. Rev. C **78**, 034311 (2008).